HHS Public Access

Author manuscript

Coord Chem Rev. Author manuscript; available in PMC 2020 January 15.

Published in final edited form as:

Coord Chem Rev. 2019 January 15; 379: 99–120. doi:10.1016/j.ccr.2017.09.002.

Metalloporphyrin Nanoparticles: Coordinating Diverse Theranostic Functions

Shuai Shao[1], **Venugopal Rajendiran**[1,2], and **Jonathan F. Lovell**[1,*]

[1]Department of Biomedical Engineering, University at Buffalo, State University of New York, Buffalo, New York 14260, USA

[2]Department of Chemistry, School of Basic and Applied Sciences, Central University of Tamil Nadu, Thiruvarur 610 005, India

Abstract

Metalloporphyrins serve key roles in natural biological processes and also have demonstrated utility for biomedical applications. They can be encapsulated or grafted in conventional nanoparticles or can self-assemble themselves at the nanoscale. A wide range of metals can be stably chelated either before or after porphyrin nanoparticle formation, without the necessity of any additional chelator chemistry. The addition of metals can substantially alter a range of behaviors such as modulating phototherapeutic efficacy; conferring responsiveness to biological stimuli; or providing contrast for magnetic resonance, positron emission or surface enhanced Raman imaging. Chelated metals can also provide a convenient handle for bioconjugation with other molecules via axial coordination. This review provides an overview of some recent biomedical, nanoparticulate approaches involving gain-of-function metalloporphyrins and related molecules.

Graphical Abstract

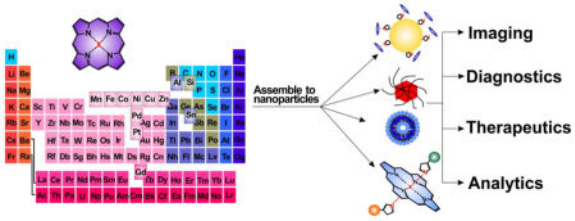

Keywords

Metalloporphyrins; nanoparticles; theranostics

* jflovell@buffalo.edu.

1. Introduction

Porphyrins and related molecules are well-suited for theranostic applications [1–5]. Metalloporphyrins have unique chemical properties which confer distinct bioinorganic function. Beyond roles in natural bioprocesses, metalloporphyrins can be used for biomedical applications. As shown in Fig. 1, by adding different metals, new capabilities can be conferred by the metal. For example, Mn- and Gd- porphyrin have been applied as magnetic resonance imaging (MRI) contrast agents; ^{64}Cu- porphyrin has been demonstrated as an efficient positron emission tomography (PET) agent; Mn-, Ni- and Fe-porphyrins show potential for use in surface enhanced Raman scattering (SERS); Pd- and Pt- porphyrin have been used as photosensitizers for upconversion nanoparticles (UCNPs), as well as components for optical oxygen sensors; Zn- and Al- porphyrin have been used for photodynamic therapy (PDT); Mn- and Fe- porphyrin have been used as superoxide dismutase (SOD) mimicking agents; Co-, Sn- and Si-porphyrin are able to participate in bioconjugation by axial coordination ligands. This review provides an overview of some of these unique nanoscale applications of metalloporphyrins.

1.1 Metalloporphyrins in Nature

The Fe^{2+} containing heme group (Fig. 2A), is not just the oxygen carrier found in hemoglobin; it is a cofactor of hemeproteins including cytochromes and peroxidases that carry out diverse biological reactions. Through shuttling electrons, these iron porphyrins catalyze oxidation and reduction reactions. Cytochrome P450, one of the most important heme enzymes, was so-named when an unexpected pigment was observed with 420 nm absorbance in microsomes during reduction in presence of carbon monoxide [6]. The pigment was later recognized specifically as a hemeprotein in 1964 [7]. Cytochrome P450 is a crucial component for catalyzing the hydroxylation of organic substrates [8]. Heme dependent peroxidases are another important group of hemeproteins, composed of single polypeptide chains with a heme complex attached by the chelation between iron and histidine, that catalyzes the breakdown of hydrogen peroxide [9].

Occurring in most plants and algae, photosynthesis converts light energy into chemical energy and is the primary source of biological energy and molecular oxygen on earth. Chlorophyll, a family of green pigments that absorb sunlight, is central to photosynthesis. It chelates a magnesium atom center (Fig. 2B). Chlorophyll is a reduced porphyrin (chlorin) macrocycle, which contains two π electrons less than porphyrin. Chlorophyll is intensely studied in biological, environmental, and agricultural, and plant sciences [10–13].

Another metal pyrrole-like macrocycle is Vitamin B_{12}, a crucial vitamin for nervous system function (Fig. 2C). It contains a cobalt atom in the center of the aromatic tetrapyrrole. Vitamin B12 is necessary for the function of methionine synthase and L-methylmalonyl coenzyme A mutase. Vitamin B12 deficiency results in megaloblastic anemia and nervous system disease [14–17]. Sea food and meat are good dietary sources of vitamin B12.

Methane is the simplest organic compound and a potential clean energy source. Methane-producing archaea produce nearly 1 billion metric tons of methane annually in the global carbon cycle [18]. Cofactor F430, a nickel-containing tetrapyrrole (Fig. 2D), is found in

methyl-coenzyme M reductase (MCR) and catalyzes the terminal step of methanogenesis. The successful biosynthesis of F430 was achieved recently and holds potential for industrial metabolic bioenergetic engineering [19].

1.2 Nanoparticles in Biomedicine

Nanoparticles hold promise for many biomedical applications [20–23]. Intravenous administration of pharmaceutical suspensions was historically avoided, given the risk of embolism, but clinical colloidal drug delivery approaches have been made possible by suitable nanoparticles, like liposomes and micelles [24]. Compared to small molecules, nanoparticles can improve drug efficiency via prolonging circulation times and reducing toxicity [25]. For some diseases like cancer, nanoparticles can accumulate in tumors due to the enhanced permeability and retention (EPR) effect [26–29]. Nanoparticles can act as efficient transport vehicles for drugs or functional molecules with potential for high loading capacity and tunable chemical and biological stability [30–33]. The high surface-to-volume ratios of most nanoparticles allows for productive surface modification by grafting biomolecules such as targeting ligands or detection probes [34]. These intrinsic properties motivate the development and design of nanoparticles as theranostic agents capable of multiple functions, such as optical imaging, bio-sensing, ligand targeting, and delivery of drugs.

2. Preparation of metalloporphyrin nanoparticles

2.1 Coordination Chemistry

Tetrapyrroles are versatile functional molecules that have found applications in chemistry, biology, medicine, and materials science [35]. As mentioned above, metals play a central role in many naturally occurring porphyrins, highlighting the significance of bioinorganic coordination chemistry. Coordination of metals in the porphyrin can enhance the stabilization of the ring, thereby promoting a more planar conformation [36] or enhance thermodynamic and kinetic stability [37, 38]. The photochemical and photophysical properties of the porphyrin can be altered by the nature of the metal atom coordinated in the porphyrin ring. Porphyrins and many of their derivatives readily form N-ligated complexes with a variety of metals by deprotonation of one or two of the pyrrole NH protons via the formation of σ bonds, either within the core or above it [39]. The nature of the bonds and orbital overlap between metal ions and the porphyrin ligand have been comprehensively reviewed [40]. Generally, σ-complexes of porphyrins are known for almost every metal cation in the periodic table. In addition to σ-complexes, a considerable number of π-complexes derived from tetrapyrrolic ligands have been recently reported [41]. This review discusses coordination chemistry of σ-complexes, especially transition metal complexes because these have been studied more frequently in metalloporphyrin nanoparticles.

When 2 protons are lost, the porphyrin core forms a dianion that acts as a tetradentate ligand, so chelated metal ions usually have a coordination number of at least 4 [42]. Importantly, π electronic delocalization, which occurs within the porphinato ligand, leads to planarity of the macrocycle and an essentially square-planar environment for the metal ion in the four-coordinate complexes. Upon addition of other ligands in addition to four coordinate

metalloporphinato core, there is a possibility of forming 4–8 higher coordination number (C.N) metalloporphyrins. The geometries of square-planar (C.N = 4), square-pyramidal (C.N = 5) and octahedral (C.N = 6) metalloporphyrins are shown in scheme 1 [42, 43]. In general, the geometry of transition metal complexes depends on the electronic configuration of the d orbital of the coordinating metal ion. In the case of four-, five- and six- coordinated first-row transition metalloporphyrins, the influence of occupied or unoccupied $3d_{x^2-y^2}$ and $3d_{z^2}$ orbitals on the bond distances of M-N and M-L is significant [42]. Relatively large M-N bond distances are observed in the case of five-coordinated metalloporphyrins compared to four and six-coordinated metalloporphyrins due to displacement of the metal atom out of the porphinato plane [42].

Other properties are also relevant besides metalloporphyrin geometry. The periodic table of metalloporphyrins, synthesis, selected metal insertion procedures, role of the metal oxidation state in the carrier, the stable oxidation states of metal ions in metalloporphyrins and optical absorption spectra are all other considerations [44]. Apart from transition metal-based metalloporphyrins, non-metallic and semi-metallic elements are also able to be chelated [45]. This includes boron and tellurium porphyrins complexes, and Group 14 (silicon and tin) and Group 15 porphyrin complexes.

2.2 Incorporation of Metalloporphyrins in Nanoparticles

Typically, chelation of metals in the porphyrin is completed prior to nanoparticle formation, although this need not be the case. In some uses, like ^{64}Cu PET imaging, post-chelation is advantageous due to the limited half-life of the radionuclide. There are other advantages of post-chelation approaches, since if chelation is possible without degradation of the nanoparticles, one single batch of nanoparticles can be divided and chelated with various metals to confer multiple functions. Metalloporphyrins can attach to the nanoparticle carrier either as encapsulated cargo or via surface modification. In this section, some common methods to prepare metalloporphyrin nanoparticles are briefly discussed.

2.2.1 Solvent Mixing—Similar to freebase porphyrins, many metalloporphyrins and derivatives are hydrophobic and soluble only in organic solvents. For the mixing solvent method, sometimes involving host–guest methods, the first step is dissolving hydrophobic metalloporphyrins (and possibly stabilizers) in organic solvents which are miscible with water such as methanol, acetonitrile, or dimethyl sulfoxide. Addition of water, which may contain surfactants, leads to colloidal self-assembly that prevents the hydrophobic metalloporphyrin core from aggregation. The organic solvents can subsequently be removed by dialysis and the final metalloporphyrin nanoparticles are transferred to a fully aqueous solution (Fig. 3A) [46, 47]. If the nanoparticles are dense enough, they may be collected through centrifugation. By cross-linking metalloporphyrin cores to the polymer matrix, the thermal stability of the nanoparticles could be improved [48]. The size and polydispersity of the obtained nanoparticles depends on the types of metalloporphyrin, the selection of surfactants, the ratio between host and guest solvents, and the reaction temperature [46, 47]. There are many possible selections for matrix polymers, such as (Polyethylene)glycol (PEG), poly(methyl vinyl ether-co-maleic anhydride) (PVM/MA), chitosan derivatives and surfactants like Tween and Pluronic. The solvent mixing method is a convenient method to

form metalloporphyrin nanoparticles. However, the process might result in leakage of metalloporphyrins from the matrix in biological settings and may be difficult to accurately control particle size and polydispersity.

2.2.2 Surface Attachment—Covalent conjugation techniques can use routine chemistry such as amide functionalization, which for example can be implemented if the surface of nanoparticles are modified with amine groups and the metalloporphyrin contains carboxylic acid groups, or vice versa [49, 50]. Non-covalent binding to nanoparticles is another strategy. Surfaces of the nanoparticles provide capacity to adsorb metalloporphyrins. Some drug delivery systems have used this approach to design metalloporphyrin nanostructures with specific features, like pH sensitivity [51] or specific electron coupling effect [52]. Mesoporous silica nanoparticles (MSNP) are a versatile system for cargo delivery through physical absorption. The high surface area and pore volume allows good loading efficiency. Besides weak electrostatic interactions, surface modification enables control of drug release during intracellular uptake or by external stimuli [53]. (Fig 3B)

2.2.3 Liposome Encapsulation—Liposome are frequently used as nanocarriers. Water-soluble metalloporphyrins can be passively loaded in the liposome aqueous core. Metalloporphyrins with poor water solubility can be loaded within the bilayer (Fig. 3C). However, loading efficiency and stability could be problematic and hydrophobic metalloporphyrins could induce over-saturated packing structure and decreased stability, especially in biological conditions. To enhance performance of liposome-loaded porphyrins, unique amphiphiles like metalloporphyrin-phospholipids have been developed. Instead of encapsulating the cargo into the liposome core or bilayer, metalloporphyrin can be pre-conjugated directly to a phospholipid side chain. In this way, the metalloporphyrin lipid self-assembles to form a lipid-like bilayer structure [54–56].

2.2.4 Dendrimers—Metalloporphyrins can be incorporated into dendrimer nanoparticles, the size of which can be precisely controlled by stepwise iterative synthesis. The structures of four different types of metalloporphyrin dendrimers are shown in Fig. 3D. Metalloporphyrins may form the core, the branch nodes, the branch terminal nodes or both the core and every node. Metalloporphyrin-cored dendrimers can be synthesized through divergent or convergent approaches. In the divergent strategy, the metalloporphyrin core is the starting point of the architecture, and branches are extended layer by layer. However, this often leads to structural imperfections in the final product. The convergent strategy pre-assembles the dendrons before attachment to the metalloporphyrin cores [57]. Metalloporphyrin dendrimers can also be combined with block copolymers [58].

3. Biomedical Applications of Metalloporphyrin Nanoparticles

3.1 Magnetic Resonance Imaging (MRI)

Since the first MR images of human body were demonstrated several decades ago, MRI has become an indispensable noninvasive diagnostic imaging technology [59]. T1 relaxation time, also known as the spin-lattice relaxation time, tends to be more important for paramagnetic contrast agents containing manganese or gadolinium, although these

paramagnetic metals reduce both T1 and T2 relaxation times. The T2 relaxation time, also known as the spin-spin relaxation time, is a more relevant signal for super-paramagnetic agents, especially iron oxide nanoparticles.

Due to the stable chelation, metalloporphyrins reduce risk of transmetallation which can cause fibrosis disorders or neurotoxicity [60, 61]. Mn(II), carrying 5 unpaired electrons and Gd(III), carrying 7 unpaired electrons, are commonly used in T1-weighted MR contrast imaging. In porphyrins, the distance between the two diagonal N is 2.9 Å. For Gd^{3+}, its ionic radius 1.08 Å plus the Gd-N average bond length 2.6 Å results in a small N-Gd-N angle, which causes higher distress and instability to the whole complex. Comparatively, Mn(II) and Mn(III) display an ionic radius of 0.6–0.7Å and an Mn-N average bond length of 2 Å indicating a more stable planar complex [62–65].

In the past 20 years, numerous studies have reported Mn-porphyrins as MRI contrast agents [66–68]. Both Mn(III)-porphyrin (7.4 mM^{-1} s^{-1}) and Mn(III)-porphyrin conjugated dextrans (8.9 mM^{-1} s^{-1}) showed a higher longitudinal relaxivity (R1) than an existing MRI agent Gd-DTPA (5.1 mM^{-1} s^{-1}), low cytotoxicity and specific binding to tumor cell membranes [69].

Pan et al. developed a self-assembled nanobialys which was labeled with Mn(III)-porphyrin as an MR contrast agent (Fig. 4A) [70]. The “bialy” nanostructure, with tunable particle size and low polydispersity, had good stability. Mn(III)-porphyrin was encapsulated in the polymeric inverted-micelle by a phase transfer process. With the addition of biotin, this toroidal-shaped nanoparticle efficiently targeted fibrin, a component of intravascular thrombosis, and offered site-specific MR T1-weighted imaging of the clot (Fig. 4B). Additionally, nanobialys showed more than 98% drug loading efficiency and more than 80% drug retention.

Another approach involved covalently conjugating Mn-porphyrins on the surface of doxorubicin (DOX)-loaded PLA nanoparticles (MnP-Dox NPs) [71]. MnP-Dox NPs were internalized by HeLa cells and suppressed cancer cell growth due to faster drug release in an acidic environment than in a neutral pH condition. As a MRI contrast agent, MnP-Dox NPs (r1 value of 27.8 $mM^{-1}s^{-1}$) exhibited enhanced relaxivity and high performance in T1-weighted MRI both in vitro and in vivo. Gradual accumulation of MnP-Dox NPs resulted in MR signal enhancement in tumors occurred 24 h after intravenous injection of nanoparticles (100 μL, 8 mg/mL). Photodynamic therapy was performed by encapsulating the free porphyrin as the photosensitizer, for MRI-guided PDT cancer theranostic nanoparticles (TPD NPs). Taking advantage of the EPR effect, TPD NPS passively accumulated in the tumor site. The PDT and MRI capabilities of TPD NPs were optimized with loading 31% freebase porphyrin and 19% Mn-porphyrin. In mice bearing HT-29 human colon tumors, after intravenous administration, the Mn-porphyrin led to enhanced MRI signal and clear T1-weighted MR images, theoretically allowing precise delivery of the laser light. After laser treatment, compared to the control groups, tumor growth was fully inhibited [50].

PLA-coated Au nanoshells were developed that were modified by Mn-porphyrin and encapsulated doxorubicin for light-triggered drug release due to NIR light absorption by the Au nanoshell (Fig. 5A) [72]. T1-weighted images of phantoms containing aqueous

dispersions of DOX@PLA@Au-PEG-MnP NPs showed MRI contrast (Fig. 5B). The signal at the tumor enhanced over time and clear and bright images of tumor structure were observed after 0.5h and 24h post-injection (Fig. 5C, 5D and 5E). This multifunctional theranostic agent combining photothermal therapy (Au nanoshell), chemotherapy (DOX) and MRI (Mn-porphyrin) could offer a synergistically improved therapeutic treatment to the cancer.

Fullerene derivatives have been combined with Mn-porphyrins [73]. By conjugating 5-(4-aminophenyl)-10,15,20-tris(4-sulfonatophenyl)porphyrin (APTSPP) to [6,6]-phenyl-C_{61}-butyric acid ($PC_{61}BA$), the obtained $PC_{61}BA$-APTSPP-Mn displayed a relaxivity of 19.2 $mM^{-1}s^{-1}$, a higher value than Mn-APTSPP (11.2 $mM^{-1}s^{-1}$) and the clinically used MRI reagent Gd-DTPA (4.1 $mM^{-1}s^{-1}$) at 0.5T. The influence of fullerene could be explained by the charge density variation of Mn(III) and steric decompression caused by $PC_{61}BA$, rather than the rotational correlation time.

Mn-porphyrin-phospholipid has been developed as a multifunctional building block (Fig. 6). MacDonald et al. developed porphysomes using Mn-porphyrin-phospholipid as both a MRI contrast agent and a photothermal sensitizer [74]. The Mn-porphyrin porphysome was composed of 95% Mn-porphyrin lipid and 5% DSPE-PEG 2000. MR relaxivity was evaluated in both intact and disrupted conditions. In the presence of detergent, the liposome structure was disrupted and increased relaxivity was observed. Although insertion of Mn quenched the generation of singlet oxygen, the Mn-porphyrin liposome exhibited resistance to bleaching and enhancement in photothermal activity. No loss of photoacoustic signal was observed in Mn-porphyrin liposome while the freebase porphyrin liposome decreased 4 folds. The enhancement in photostability ensured good performance of Mn-porphyrin liposome in repeated photothermal treatments without loss in heat production.

Based on a similar idea, Keca et al. reported Mn-texaphyrin phospholipid for MRI. Texaphyrin, a larger pyrrole-based macrocycle, offers pentadentate coordination for metal chelation with one more coordinator compared to the 4-coordination model in porphyrins [75]. The additional coordination could result in improved chelation stability in some cases. Enhanced visualization of lymphatic drainage from the tumor site to adjacent lymph nodes was detected after rabbits were injected with Mn-nanotexaphyrin (8 mg/ml, 1.5 mL) (Fig. 7A).

In Mn-porphyrin-phospholipid liposomes, increased relaxivity is observed when the intact bilayer is disrupted by detergent [74]. This suggests that increased water access within the bilayer could enhance MRI contrast performance. 2-[1-hexyloxyethyl]-2-devinylpyropheophorbide-a (HPPH) is a porphyrin derivate that has been used for photodynamic therapy [77]. Liposomes formed from HPPH-lipid were demonstrated as chemophototherapy agents with laser-trigger drug release [78]. Shao et al. reported the synthesis of an amine modified N-HPPH-lipid with the terminal of the HPPH side chain modified by the amine group [76]. Due to hydrogen bonding between the amine group and water molecules, water content in the hydrophobic bilayer was enhanced. This was shown with molecular dynamic simulation (Fig. 7B and 7C), X-ray diffraction and electron spin resonance analysis. The modified N-HPPH-lipid film could be solubilized rapidly with water

but the HPHH-lipid film barely dissolved (Fig. 7D). In intact liposomes, this amine modification resulted in 150% higher T1 relaxivity $(mM\ s)^{-1}$ due to the higher water content in the bilayer. When the structures were disrupted by detergent, the Mn-HPPH-liposome and Mn-N-HPPH liposome exhibited almost equal T1 relaxivity. Increased MR signal in blood and liver was observed following intravenous injection and no acute toxicity was observed.

The Mn-N-HPPH-lipid and Mn-texaphyrin-phospholipid liposomes are two examples demonstrating the potential application of Mn-porphyrin-phospholipid liposome used in vivo. In addition, considering porphyrin liposomes have been demonstrated as a carrier of water soluble molecules and chemophototherapeutic agents [79–84], Mn-porphyrin liposomes hold potential to be an inherently multifunctional theranostic agent with MRI, photoacoustic, chemotherapy, photothermal therapy and photodynamic therapy properties.

Although Gd-porphyrin chelation stability may not be highly robust, a series of Gd-porphyrin molecules was synthesized as T1-weighted MRI enhance contrast agents. Jahanbin et al. developed a MRI contrast agent by conjugating gadolinium meso-tetrakis(4-pyridyl)porphyrin [Gd(TPyP)] to chitosan [85]. The Gd(TPyP) was passively absorbed into optimized chitosan nanoparticles with a narrow size distribution of 35–65 nm. No evident distortion was observed during the encapsulation process and the loading capacity Gd(TPyP) was 87%. MRI experiments showed that Gd(TPyP) chitosan nanoparticles had T1 relaxivity of 38.35 $mM^{-1}s^{-1}$, 12 fold higher than the conventional Gd-based MR contrast agents such as Gd-DOTA (~4 $mM^{-1}s^{-1}$ at 3T).

Gong et al. reported a multifunctional polymeric micelle system containing a NIR dye, IR825 and chlorin e6 (Ce6), a photosensitizer which additionally served as the Gd^{3+} chelator (Fig. 8A) [86]. This nanoparticle displayed 7 times higher r_1 value than Magnevist, a clinical Gd-based T1-weighted contrast agent (Fig. 8B). In animal experiments, triple-modal fluorescence, MR and photoacoustic imaging demonstrated efficient accumulation occurred in the tumor site via the EPR effect (Fig. 8C). Inhibition of the tumor growth was achieved with the combination of photothermal and photodynamic therapy. These properties demonstrate the capability of porphyrin nanoparticles for multimodal imaging and image guided treatments [87, 88].

The weaker chelation stability of Gd in porphyrins has likely limited their use as chelators for MR agents. Liang et al. developed a facile one-step aqueous dispersion polymerization to fabricate polypyrrole nanoparticles from a mixture of pyrrole and pyrrole-1-propanoic acid [89]. Gd was subsequently attached using a DOTA chelator with a polyethylene glycol linker. The obtained PEGylated poly-pyrrole nanoparticles conjugating gadolinium chelates (Gd-PEG-PPY NPs) displayed a high T1 relaxivity coefficient of 10.6 $mM^{-1}s^{-1}$, more than twice as high as Gd-DOTA at 3T magnetic field. Clear MR images of tumors were observed in mice bearing U87-MG tumors after intravenous administration of Gd-PEG-PPY NPs (100 μL, 5 mg/ml).

Due to improved coordination, Gd(III)-texaphyrin compounds, developed by the research group of Sessler, are more stable in vivo than the corresponding Gd(III)-porphyrin analogues [90–92]. Polymer micelles encapsulating Gd-texaphyrin as an MRI contrast agent have been

described [93]. Multiples copies of specific ligands for the melanocortin 1 receptor (MC1R), a cell-surface marker for melanoma, were stabilized through the Fe(III) cross-linking. These ligand-Gd-texaphyrin micelles demonstrated effective targeting to the MC1R-expressing xenograft tumors based on MR images

Another Gd-porphyrin theranostic nanoparticle was reported by Lee et al. [94]. Through a disulfide bond, Dox was conjugated with Gd-texaphyrin and resulted in Dox fluorescence quenching. Gd-texaphyrin offered MRI guidance for tracking the compound. In the presence of glutathione, the bonds were cleaved and the recovery of fluorescence at 592 nm was observed as the signal of release of free DOX. The Gd-texaphyrin conjugated Dox could be encapsulated into folate-receptor-targeted liposomes (Fig. 9). Liposomal Gd-texaphyrin showed specific uptake and cleavage to release DOX, which enhanced antiproliferative effects in cancer cells overexpressing the folate-receptor. Reduction of tumor burden was observed in two mouse tumor models (metastatic liver cancer orthotropic model and a subcutaneous KB cell xenograft model). This theranostic nanoparticle also presented enhanced T1-weighted MR imaging in vivo for detection metastatic cancer progression at the early stage.

Iron oxide compounds are often used as superparamagnetic nanoparticles (SPIONs). This type of contrast agent shortens the T2 relaxation time for T2-weighted MRI. Zn-porphyrin modified Iron oxide nanoparticles have been developed as multifunctional theranostic agents. Yoon et al. reported a layer-by layer self-assembled polymeric nanocapsule with a SPION core and a dendrimeric Zn-porphyrin shell (Fig. 10A) [95]. PEGylation provided the nanocapsule with water-solubility and the NCs displayed adequate magnetic character (>20 emu/g) for MRI applications with a T2 relaxivity (r_2) value of 93.5 $mM^{-1}s^{-1}$. In another approach, Zn-porphyrins were used with dextran SPIONs [96]. The Zn-porphyrin was covalently conjugated with the dextran-based paramagnetic nanoparticles by “click” reaction. Zn-porphyrin was used instead of the freebase porphyrin since the copper used during the “click” reaction would chelate the freebase porphyrin and result in quenched porphyrin fluorescence and singlet oxygen generation. The grafting of cationic Zn-porphyrin resulted in an increased r_2 value around 245 $mM^{-1}s^{-1}$ and a high r_2/r_1 relaxivity ratio up to 27 indicating this Zn-porphyrin modified magnetic dextran nanoparticle was an efficient T2 contrast agent. This is a unique example in which a metal porphyrin was selected to prevent the chelation of another metal (copper) during synthetic reaction in order to preserve desirable fluorescence and singlet oxygen generation properties.

Phthalocyanines can form coordination complexes with zinc (ZnPC). Boudon reported a SPIO-phthalocyanine nanoparticle as a magneto-optical agent (Fig. 10B) [97]. By consecutively coating each layer, a high yield of up to 30% ZnPC grafting to the SPIO surface was achieved due to the low steric hindrance of the neighboring ZnPC and short PEG chains. This SPIO-ZnPC nanoparticle was demonstrated as a T2 MRI contrast agent with an r_1 value of 3 $mM^{-1}s^{-1}$ and an r_2 value of 73 $mM^{-1}s^{-1}$ (r_1/r_2 =24). Xuan et al. reported the design of highly magnetized silica-coated porous microspheres with porous γ-Fe_2O_3 core in which the size of magnetic core and the shell thickness could be controlled and optimized by tuning the synthetic parameters (Fig. 10C) [98]. Hydrophobic ZnPC was

encapsulated in the microsphere and this nanoparticle displayed an r_2 value of 76.5 $mM^{-1}s^{-1}$.

3.2 Positron Emission Tomography (PET)

Single-photon emission computerized tomography (SPECT) and positron emission tomography (PET) are commonly used clinically for non-invasive, imaging diagnosis of human diseases [99]. Although both have advantages and disadvantages, compared to SPECT, PET has greater sensitivity and resolution [100]. In general, porphyrins have been widely explored as radionuclide chelators[101]. Although there have been some recent examples of using porphyrins for chelation and imaging of SPECT tracers such as ^{111}In and ^{99m}Tc [102, 103], we will focus on nanoparticulate PET approaches.

Porphyrins and phthalocyanines are promising PET agents as they are also NIR fluorophores, are biologically compatible, metal complexes are thermodynamically and kinetically stable, and they usually exhibit some specificity for tumors, with or without the presence of a coordinated metal in the central core [104–106]. Cu-phthalocyanine was described as a ^{64}Cu chelator that accumulated in rodent brain tumors as early as 1951 [107]. The physical properties and availability of ^{64}Cu make it a useful nuclide for PET imaging: $t_{1/2}$= 12.7 h, β+: 17.4%, $E_{\beta+max}$ = 656 keV [108]. The in vivo pharmacokinetics and biodistribution of porphyrins are generally not altered by chelation with ^{64}Cu [108–110].

The Zheng group investigated incorporating ^{64}Cu into a porphyrin-peptide-folate (PPF) probe as a folate receptor (FR) targeted fluorescent/PDT agent [111]. ^{64}Cu-PPF uptake in FR-positive tumors was apparent with small animal PET with a high tumor-to-muscle ratio of 8.9 observed after 24 h. Competitive blocking studies confirmed the specificity of the FR-mediated tracer uptake in the tumor. This concept was advanced from peptide to nanoparticle, when it was discovered that organic porphysome nanoparticles could function as seamless ^{64}Cu radiotracers [112]. Incubation of ^{64}Cu with pre-formed nanoparticles in appropriate conditions resulted in a fast (30 min), one-pot, high yielding (>95%) procedure producing stable radiolabeled nanoparticle (Fig. 11A) The intrinsic ability of the porphysomes to directly chelate ^{64}Cu allows them to be accurately and noninvasively tracked in vivo. Only a fraction of the porphyrin-lipid bilayer is directly labeled with copper, thereby preserving NIR fluorescence properties. This approach was used for tracking and real-time delineation of orthotopic prostate tumors and micrometastases [113]. This successful application of ^{64}Cu-porphysomes in clinically relevant orthotopic and metastatic cancer models is promising for translation. Clear multimodal delineation (using both PET and fluorescence) of orthotopic tumors on both the macro- and the microscopic scales was observed, as was sensitive detection of small metastases (<2 mm) (Fig. 11B, 11C and 11D).

Porphyrin-phospholipid can also be used to coat existing nanoparticles and confer seamless PET labeling and contrast. This strategy was adopted by using porphyrin-phospholipid to coat UCNPs. This simple approach yielded nanoparticles that could be used in 6 different imaging modalities, including Cerenkov luminescence and PET imaging, which were enabled by ^{64}Cu labeling (Fig. 12A) and lymphatics imaging was demonstrated (Fig. 12B) [114]. Expanding the concept of seamless ^{64}Cu labeling for multimodal imaging, a porphyrin polymeric mesh was developed using tetracarboxylic porphyrins and PEG

diamines as polymer monomers [115]. Following intravenous administration the porphyrin mesh was rapidly cleared via renal excretion in healthy mice but not mice suffering from rhabdomyolysis acute renal failure. Renal clearance was monitored by fluorescence analysis and seamless whole body ^{64}Cu PET imaging. In another example, surfactant-stripped micelles were developed from pheophytin or naphthalocyanines that results in micelles with very high cargo-to-excipient ratios [116, 117]. These micelles can be seamlessly labeled with ^{64}Cu for whole body gut imaging.

Li et al. developed a versatile 'all-in-one' porphyrin-based organic nanoconstruct termed nanoporphyrin that was self-assembled with a single organic building block, a porphyrin/cholic acid (CA) hybrid polymer (Fig. 13A) [118]. PET imaging following seamless ^{64}Cu labeling showed the nanoporphyrin started to accumulate at tumor sites 4 h after injection, and reached maximum level at 16 h. After 24 h, the radiolabel was found primarily at the implanted tumors, with low background in the rest of the body (Fig. 13B). The versatility of the approach was extended by developing dual-modality nanoprobes by synergistically combining PET and MRI to provide accurate diagnoses. Both ^{64}Cu(II) and Gd(III) could be efficiently incorporated into nanoporphyrin for both MRI contrast and PET tumor imaging [118]. Heterogeneous tumor uptake distribution was revealed using PET-MRI (Fig. 13C) [118].

Feng and colleagues used a liposome approach with a sequential activation pattern by encapsulating a hydrophobic photosensitizer chlorin e6 (Ce6) into the bilayers and AQ4N into the aqueous cavity of PEGylated liposomes [119]. The AQ4N-Ce6-liposome demonstrated hypoxia-dependent cytotoxicity and photodynamic cell killing ability. In addition to its inherent contrast with fluorescence and photoacoustic imaging, seamless ^{64}Cu chelation conferred capabilities as a PET imaging probe. After intravenous injection of AQ4N-^{64}Cu-Ce6-liposomes into BALB/c mice bearing 4T1 tumors (~10 MBq per mouse), the liposomes accumulated in tumors. Ex vivo distribution was carried out by recording the radioactivity extracted tissues. Tumor accumulation was measured to be 4.7 % ID g^{-1}, comparable to the in vivo PET imaging analysis. This approach shows not only that can PET imaging non-invasively assess pharmacokinetic and time-dependent biodistribution, but the use of porphyrin nanoparticles has the advantage of having the option to use ^{64}Cu to conveniently gain critical information about pharmacological behavior.

3.3 Optical Imaging

3.3.1 Surface Enhanced Raman Scattering (SERS)—Surface enhance Raman scattering (SERS) based on gold nanoparticles (AuNPs) is a promising technique for bioanalysis and diagnosis [120–123]. By analyzing Raman signatures, highly multiplexed analysis of nanoparticles is possible. Porphyrins are potential SERS agents [124]. SERS analysis can be used to understand how various metalloporphyrins (e.g. Fe, Ni, Cu) interact on the surface of AuNPs [122]. 5,10,15,20-Tetra(4-pyridyl)-21H,23H-porphine metallocomplexes (M-TPyP, M=Cu, Fe. Ni) were linked onto AuNPs surfaces in various proportions to form well-ordered monolayers for analysis.

Phospholipid coating can enhance AuNP stability and biocompatibility for biological application [125]. However, the strong fluorescence of freebase porphyrin can interfere with

SERS signal detection. Tam et al. reported that fluorescently quenched Mn-porphyrin phospholipid could be used as both a stabilizing, biocompatible surface coating agent and Raman dye to encapsulate the AuNPs for SERS imaging (Fig. 14A) [126]. Mn-porphyrin lipid coated AuNPs showed clear uptake in A549 lung cancer cells based on Raman micrographs (Fig. 14B). This is the first use of porphyrins as a SERS reporter molecule in contrast enhanced imaging and offers convenient control of the Raman dye amount absorbed on the AuNPs.

Similar to Mn-porphyrin phospholipid, palladium-porphyrin phospholipid (PdPL) was also reported for SERS imaging, when coupled with plasmonic nanoparticles [127]. The obtained PdPL-NPs can serve both as SERS reporters and PDT photosensitizers at the same wavelength (638nm), allowing the potential real-time monitoring of photosensitizers in vivo through the SERS signal. Compared with fluorescence tracking of photosensitizer, SERS eliminates reliance on fluorescence so that the absorbed light energy can be fully directed towards enhanced PDT efficacy.

3.3.2 Photoacoustic Contrast—Porphyrins and its derivatives have been evaluated and successfully utilized as the contrast agents in photoacoustic (PA) imaging [56, 128, 129]. Recently, Ng et al. reported a novel design of metalloporphyrin for the photoacoustic application [130]. The Zn-porphyrin was modified with a formyl side chain and conjugated to a hydroxyl lysolipid. The obtained Zn-MeO-porphyrin lipid self-assembled into a bilayer structure, improving colloidal stability (Fig. 15A). The advantage of using Zn-porphyrin instead of free-base-porphyrin was that within the lipid bilayer structure, the Zn formed the coordination with MeO group resulting in a 72 nm bathochromic shift in the Q_y band. This shift was not observed in its monomeric state, or in presence of detergent. In addition, circular dichroism demonstrated the presence of active chiral Zn-porphyrin structure within the bilayer (Fig. 15B). PA imaging of 20% Zn-MeO-chlorin-lipid nanovesicles was detectable in the tumor-bearing mice after intravenous administration (Fig. 15C). An obvious increase in PA signal was observed 5 min after the administration of Zn-MeO-chlorin-lipid nanovesicles (Fig. 15D).

3.3.3 Upconversion Sensitizer—Chelation of heavy metal atoms into porphyrins, such as palladium (Pd) or platinum (Pt), enhances the triplet state conversion and phosphorescence. For example, the Pd-TPP has a quantum yield of phosphorescence of $\Phi P=0.17$ whereas the freebase TPP has a quantum yield $\Phi P=4\times10^{-5}$,. Upconversion luminescence is an anti-Stokes energy process and offers distinct advantages in bio-imaging, including elimination of background fluorescence from both endogenous chromophores and conventional fluorescent probes [131–133]. One of the preparation strategies of the UCNPs is based on triplet–triplet annihilation (TTA) upconversion. Due to the independent selection of the sensitizer and annihilator, compared with UCNPs prepared by rare-earth-based materials co-doped with Yb^{3+} and Er^{3+}, TTA upconversion nanoparticles (TTA-UCNP) could be designed with adjustable and tunable excitation and emission. A benzene solution of Pt(II) tetraphenyltetrabenzoporphyrin (sensitizer) and BODIPY dye showed a TTA-based ΦUCL of 15 % which is higher than many Yb^{3+} based UCNP [134].

Liu et al. reported successful fabrication of water-soluble TTA-UCNP with ΦUCL of 4.5% in aqueous solution by coloading a photosensitizer (Pd-octaethylporphyrin) and annihilator (9,10-diphenylanthracene) into silica nanoparticles (Fig. 16) [135]. This TTA-UCNP showed good photostability and low cytotoxicity. In vitro confocal imaging in live Hela cells and in vivo lymphatic imaging showed that TTA-UNCP could be applied for upconversion luminescence imaging with high signal-to-noise ratios.

The same group reported another TTA-UCNP using Pt(II)-tetraphenyl-tetrabenzoporphyrin (PtTPBP) and BODIPY dyes (BDP-Green and BDP-Yellow) (Fig. 17A) [136]. The TTA-UCNP was prepared by loading both sensitizer and annihilator into BSA–dextran stabilized oil droplets, instead of the previous used SiO_2-coating nanosystems which gave a weak UCL emission (ΦUCL < 0.1%) due to the aggregation-induced fluorescence quenching of annihilators. The BSA–dextran stabilized oil droplets system achieved better upconversion efficacy (ΦUCL for BDP-Green UCNP =1.7% and ΦUCL for BDP-Yellow UCNP =4.8%) by maintaining high translational mobility of chromophores to avoid the aggregation-induced luminescence quenching. The obtained the TTA-UCNP could be used as a potent probe for in vivo lymph node imaging of mice (Fig. 17B).

3.4 Photodynamic Therapy (PDT) Agents

Photodynamic therapy (PDT) is a photoablative technique that has been used for the treatment of various solid tumors. Upon excitation with a specific wavelength of laser irradiation, an activated photosensitizer (PS) can interact with molecular oxygen to produce reactive oxygen species (ROS) including singlet oxygen ($^1O_2$), hydroxyl radicals (•OH) and superoxide (O_2^-) ions resulting in cell death and tumor destruction [137–139].

Zn-porphyrins have been used extensively in the PDT. As a suitable NIR emitting fluorophores, most Zn-porphyrin or Zn-phthalocyanine photosensitizers have an excitation band in the 650–800 nm range, a fluorescence quantum yield ΦF= 0.04–0.3, and a molar extinction coefficient around $\varepsilon = 10^5\ M^{-1}cm^{-1}$ [140–144]. Additionally, the stable chelation between Zn and porphyrin molecules protects the fluorescence from being quenched due to the unexpected chelation of other metals, like the Cu.

PEGylated SPIONs containing Zn-porphyrin generated intracellular ROS after the light irradiation. And using the HeLa cells as a model cell line, cellular phototoxicity experiments showed decreasing cell viability as a function of irradiation time and the numbers of Zn-porphyrin coated layers [95]. The PDT effect of serial Zn-porphyrin magnetic dextran nanoparticles (PS/MNP) was evaluated against the HaCaT cell line. The neutral and cationic PS/MNPs, but not the ionic ones exhibited high cell-uptake and cytotoxicity after irradiation. The confocal microscopy presented a relative colocalization of Zn-porphyrin and mitochondria indicating the PS/MNPs leaded to the tumor cell death by intrinsic apoptotic pathway and subsequent elimination by phagocytosis [96].

Hydrophobic zinc(II) phthalocyanine (ZnPC) was encapsulated into magnetic microspheres composed of porous γ-Fe_2O_3core and porous SiO_2 shell. Due to the large BET surface area 222.3 m^2/g, the biocompatible microsphere with 170 nm size showed the loading capacity of ZnPC up to 53 mg/g. The ZnPC microspheres were demonstrated to be internalized by T29

human colorectal carcinoma cells and showed 80% cytotoxicity with the light irradiation [98].

A common problem and dose-limiting factor associated with PDT is undesired acute phototoxicity during treatment or sunlight phototoxicity following treatment. Carter et al. reported a detailed study on the therapeutic activity of metalloporphyrin-phospholipid liposomes based on HPPH-phospholipid conjugates. Cu(II) or Zn(II) was chelated into the HPPH-phospholipid [145]. Compared with the freebase HPPH liposome, Cu chelation quenched more than 90% fluorescence and significantly reduced the generation of singlet oxygen, thereby attenuating all PDT efficacy. The Zn-HPPH liposome retained fluorescence and generation of singlet oxygen allowing it to permeabilize tumor vasculature and enhance delivery of mitoxantrone to the target tumor. Uniquely, the Zn-HPPH-lipid liposome exhibited strong self-bleaching effects under laser irradiation, thereby reducing phototoxicity. Photobleaching was observed in mice treated with laser irradiation at 24h post-injection with Zn-HPPH-lipid liposome compared to the freebase ones (Fig. 18). Lethal phototoxicity occurred with freebase, but not Zn HPPH liposome phototreatment. Zn-HPPH-lipid was used as an efficient antitumor drug carrier in vivo with light-triggered release with eliminated phototoxicity.

In another example, ZnPC was encapsulated into poly (D, L latic-co-glycolic acid) (PLGA) PLGA nanoparticles with 70% efficiency using a solvent emulsion and evaporation method [146]. 15% of the ZnPC rapidly released in the first 3 days and another 25% released more slowly during a period of 25 days. In vitro, up to 60% cell death was observed in P388-D1 cells treated with the combination of ZnPC-PLGA nanoparticle and light irradiation.

Some chelated metals in porphyrins can form metallosupramolecular coordination complex with the other molecules, like histidine. Yao et al. designed a dual pH sensitive MSNP in which the PEGylated tetraphenylporphyrin zinc (ZnPor-CA-PEG) was used as the “gate keeper” to control the release of loaded drug [147]. The ZnPor-CA-PEG formed a metallosupramolecular-coordination complex, preventing the loaded drug from leaking out, with the histidine grafting on the surface of silica nanoparticles. In extracellular environments where the pH was ~6.8, the binding between acid sensitive cis-aconitic anhydride (CA) and ZnPor was cleaved resulting in cellular internalization of the nanoparticles. Cellular internalization of the MSNP-ZnPor-CA-PEG was demonstrated by confocal laser scanning microscopy. The metallosupramolecular-coordination complex was broken down in intracellular acidic microenvironments (pH~5.3) to release drugs like DOX. ZnPor and the released Dox offered the combination the chemotherapy and PDT (Fig. 19A). In vitro, in Hela and MCF-7 cell lines, the treatment of Dox-loaded MSNP-Por-CA-PEG with irradiation displayed the highest cytotoxicity compared with control groups. The combination of chemotherapy and PDT has emerged as a promising treatment modality for solid tumors [148].

Based on similar principles, using metallosupramolecular-coordination complexation between ZnPor and histidine, a novel metallosupramolecular nanogel (SNG) loaded with Dox was designed by the same research group (Fig. 19B). The Dox-loaded ZnPor-SNG responded to the intracellular acidic environment to release the ZnPor and DOX. Both in

vitro and in vivo experiment revealed that the Dox-loaded ZnPor SNG with irradiation was an more efficient antitumor treatment than the single chemotherapy of free doxorubicin (DOX) or photodynamic therapy of Zn-Por in SNG [51].

Like Zn, the chelation of aluminum (Al) only partially quenches the fluorescence and singlet oxygen, allowing applications for PDT. Many reported Al photosensitizer are Al-phthalocyanine based agents, including the clinically-used sulfonated photosensitizers [149]. Muehlmann reported poly(methyl vinyl ether-co-maleic anhydride) nanoparticles (PVM/MA NPs) loaded with aluminium-phthalocyanine chloride (AlPc) [150]. The association of AlPc with PVM/MA NPs was based on solvent displacement in the presence of 1.5% Tween 20 to prevent the precipitation of AlPc. At an initial AlPc concentration of 10 μM, association efficiency reached 30%. Due to the nanostructure, water dispersion of AlPc was enhanced resulting strong fluorescence and better photochemical performance. In vitro PDT with 4T1, NIH/3T3 (murine) and MCF-7 (human) cancer cells demonstrated photocytotoxicity of AlPc NPs at 0.25 μM concentration. Interestingly, in absence of light, the cytotoxicity of AlPc at high concentrations was observed in cancerous cell lines but not MCF-10A cells which represent normal breast tissue. At lower laser energy density (0.48 J/cm^2), apoptosis was predominant in via typical oxidative stress-induced apoptosis pathways. Higher laser energies density destroyed cell structures, like the cell membrane, resulting in a predominant mechanism of cell death by necrosis, which additionally induces inflammatory response that can be useful against the remaining tumor cells.

One determining factor for an effective photosensitizer is the penetration depth of the excitation light. Most porphyrin-based photosensitizers use a visible light absorption band between 600–700 nm. Upconversion nanoparticles (UCNPs) are an emerging nanomaterial that can absorb lower-energy, further red-shifted, NIR irradiation, which has deeper penetration depth, and convert it to higher-energy visible light for photosensitizer excitation [151]. Tetracarboxylic aluminum phthalocyanine AlC_4Pc has been used as a photosensitizer with MSNPs [152] and can be encapsulated inside the silica shell of UCNPs [153]. These UCNP@SiO_2(AlC_4Pc) generated singlet oxygen efficiently under NIR light. Generation of singlet oxygen from UCNP@SiO_2(AlC_4Pc) occurred under 980 nm laser irradiation (500 $mWcm^{-2}$). In vitro experiments showed NIR-induced photodynamic cytotoxicity of UCNP@SiO_2(AlC_4Pc) against murine liver cancer cells. Up to 40% cell death was observed in the group treated with UCNP@SiO2(AlC4Pc) and 980 laser irradiation for 5 minutes.

Cui et al. reported ZnPc modified upconversion nanoparticles as a theranostic agent [154]. Folate-modified amphiphilic chitosan (FASOC) was coated on the surface UCNPs and enabled the encapsulation of ZnPc with high loading efficiency. In vitro confocal and NIR imaging demonstrated the enhanced specific uptake of the UCNPs in cancer cells overexpressing the folate receptor. The UCNPs, absorbing 980 nm irradiation, efficiently transferred energy to activate ZnPc. In 1 cm tissue, the UNPCs displayed a higher production of singlet oxygen under 980 nm excitation light than that under 660 nm excitation light (which directly can excite ZnPc, Fig. 20). In vivo fluorescence imaging demonstrated targeting and active accumulation of FASOC-UCNPs in Bel-7402 tumors in nude mice. When 1 cm pork tissue was placed on top of the skin over the tumors site, improved PDT was observed with 980 nm treatment compared to the 660 nm treatment.

When irradiated through 1 cm tissue, tumor inhibition was 18% with 660 nm excitation, but 50% with 980 nm excitation. Thus, FASOC-UNPC-ZnPc represents a platform for targeted drug delivery and deep-tissue PDT.

3.5 Axial Coordination

Si, Sn and Co chelates offer additional options to impart structure to porphyrin assemblies through axial coordination. This is illustrated in Fig. 21, in which a silicon(IV) phthalocyanine was connected with two separate axial ligands to impart photosensitizer responsiveness to two separate biological stimuli through with cleavable axial quenching ligands [155].

Axial coordination of metalloporphyrins can operate on pre-formed nanoparticles and can potentially avoid exposure to organic solvents and chromatography purification. Shao et al. reported stable chelate binding between polyhistidine-tagged (his-tag) proteins and cobalt-porphyrin via the metal axial coordination [156]. The Co-porphyrin was conjugated with lysophospholipid to obtain Co-porphyrin-phospholipid (Co-PoP) and further self-assembled into liposomes in the aqueous condition where the Co-porphyrin stayed in the hydrophobic layer (Fig. 22A). After aqueous incubation with Co-PoP liposome, his-tagged polypeptides or proteins were anchored into liposome bilayer via the his tag. The attachment of protein was demonstrated by the fluorescence images of electrophoretic mobility shift assay (Fig. 22B). This binding between histidine and Co-PoP via the axial coordination showed enhanced stability both in the presence of excessive competitors (imidazole) and in biological conditions (50% serum). In addition to the kinetic inertia of Co(III), the protection provided by the liposome structure was another factor of the stable axial coordination between CoPoP and histidine since the binding occurred within the sheltered hydrophobic bilayer. Using this approach, the Co-PoP liposome was modified with his-tag RGD peptide and the obtained ligand-targeted liposomes and also used as an antigen delivery system for peptides. This approach also offers good potential for use as an antigen delivery system for proteins [157].

Fullerene has been explored as a building block for nanostructured agents due to its small size, distinct shape and unique physicochemical properties. Dyads and triads composed of fullerene complexes with coordination assemblies of metalloporphyrins have been reported for effective photoinduced charge transfer (CT) agents with long-lived charge-separated states [158–161].

Even without surface modification, fullerene can form coordination bonds with metalloporphyrins. Many different central metal porphyrins have demonstrated coordination with neutral fullerene [162–164], especially Fe-porphyrins which form the strongest bonding to neutral fullerenes among metalloporphyrins of the first-row [165]. Cobalt(II)-tetraphenylporphyrin (CoTPP) formed an axial coordination complex with ionic fullerene due to Co-C(fullerene^{-}) bonds, however, other metals such as zinc, manganese or copper failed to form such stable metal-carbon bonds. A series of CoTPP-C_{60}^{-} complexes was developed, and due to strong exchange interaction, reversible transitions from diamagnetic to paramagnetic state were observed in some compounds when dissociation occurred between CoTPP and C_{60}^{-} as the temperature increased [166–168].

The surface of fullerene can be modified with aromatic molecules containing nitrogen atoms, such as imidazolesor pyrroles, and become the axial coordination ligand for metalloporphyrins. Konarev at el reported a pyrrolidinofullerene DP3FP and its triad complex with two Mn^{II} tetraphenylporphyrins (Mn^{II} TPP) [169]. Through microwave-assisted synthesis, DP3FP could be easily and quickly prepared with two chelating pyridyl groups. The DP3FP could be considered as the axial coordination ligands and form well-ordered complexes with two Mn^{II}TPP at the same time. X-ray single crystal diffraction showed that the lengths of axial coordination Mn–N(DP3FP) bonds for both Mn^{II} TPP was 2.2 Å. The chelation resulted in distortion of the porphyrin rings to an umbrella shape with the Mn displaced by 0.4 Å out of the porphyrin plane. Optical experiments demonstrated very weak electronic interactions between the porphyrin and pyrrolidinofullerene and absence of charge transfer in the ground state in the DP3FP Mn^{II} TPP complex (Fig. 23A).

Ince et al. reported on non-covalent and covalent donor-acceptor systems based on Zn porphyrin-C_{60} fullerene derivatives [52]. Compared to covalent conjugation, axial coordination ligand showed a nearly nanosecond radical ion pair state (0.78 ns) indicating good electronic coupling between the excited state electron donor and the ground state electron acceptor. However, no electron transfer was observed in the covalent conjugation compounds, demonstrating poor electronic coupling through covalent binding. This study revealed that dyads composed of fullerene and metalloporphyrin through axial coordination can potentially form better photoactive materials.

Song et al. developed a porphyrin-fullerene dyad axial coordination reaction by combining pyridyl-modified C_{60} with equimolar tetraphenylporphyrinozinc (ZnTPPH) in hexane at room temperature (Fig. 23B) [170]. Due to the strong intramolecular electron transfer between the photoexcited ZnTPPH to its axial ligand C_{60}, the ZnTPPH-fullerene dyad showed a 71% decrease of the intensity compared to that of the 1:1 mixture of ZnTPPH with fullerene. A five-component system consisting of an electron donor (EDTA), this ZnTPPH-fullerene dyad, an electron mediator MV^{2+}, catalyst colloidal Pt, and a proton source (HOAc), was designed to investigate photoinduced H_2 evolution. With 4 h irradiation, the turnover number of H_2 evolution using ZnTPPH-fullerene dyad could reach 73, which was much higher than that of the ZnTPPH alone (2.3). H_2 evolution was not observed in the absence of any one of these five components, or without irradiation.

3.6 Superoxide dismutase (SOD) Mimicking Agents

Cell death via ROS induced by metalloporphyrins with superoxide dismutase (SOD) activity has been studied. By converting intracellular $O_2^{\cdot-}$ into H_2O_2, DNA damage can be induced which induces cell death. Fe-porphyrin was demonstrated as a promising SOD mimic with significant cytotoxicity [171, 172]. However, suitable carriers could benefit in vivo delivery of SOD mimetics. pH-sensitive liposome mainly composed of phosphatidylcholine (DMPC) and cationic/anionic lipid combination have been designed for this purpose. It could deliver the Fe-porphyrin into the cytosol when exposed to the acidic environments of the endosome [173–175]. The strong electrostatic interaction between the cationic Fe-porphyrin and the ionic lipid head could remain intact in vivo. The liposome carrier with 30 nm size enhanced the cell uptake of the Fe-porphyrin compared to the free Fe-porphyrin delivery. It showed

high cytotoxicity without phototoxic effect towards the Lewis lung carcinoma cell line and MKN28 cell line.

Besides Fe-porphyrin, Mn-porphyrin has been recognized as another potential SOD mimic for anticancer therapy. The Mn-porphyrin modified liposome has been demonstrated as an antioxidative agent for both SOD and peroxidase (POD) [176]. Various types of phospholipids, such as 1,2-distearyl-sn-glycero-3-phosphocholine (DSPC),1,2-dimyristoyl-sn-glycero-3-phosphocholine (DMPC), 1,2-dipalmitoyl-sn-glycero-3-phosphocholine (DPPC), and1,2-dilauroyl-sn-glycero-3-phosphocholine (DLPC) were used as the major lipids to form liposomes to optimize the maximum SOD and POD activity. The DMPC-based Mn-porphyrin modified liposome produced higher SOD activity, which was due to the well-dispersed ligand on the membrane in the liquid crystalline phase, and maximal POD activity which was due to cluster type of Mn-porphyrin on the membrane in the gel phase. Liposomes combined with Tween-80 and retaining Mn-porphyrins could act as SOD agent that could absorb the ApoE. By taking advantage of ApoE-induced transcytosis, it could be delivered across the blood brain barrier and the Mn-porphyrin was observed in preliminary in vivo experiment [177].

Stearate-modified Mn-porphyrin could be formulated with an alginate hydrogel carrier matrix system and formed particles around 130 nm in size (Fig. 24) [178]. This orally administered drug delivery system protected the Mn-porphyrin pass through the acidic gastrointestinal environment for intestinal delivery and resulted in antitumor effects by the $O_2^{\cdot-}$ inhibitory activity of the Mn-porphyrin. However, the total Mn-porphyrin encapsulation efficiency was only 2%.

3.7 Oxygen sensing

The sensing of biological analytes is a promising topic for metalloporphyrins [179]. As demonstrated above (Fig. 21), axial ligation can impart analytical sensing functionality to metalloporphyrins. Various metals are emerging as sensors; for example, Si impart reversible pH-responsive fluorescence [180]. However, oxygen sensing with Pd- and Pt-porphyrins is one of the most well-established sensing approach.

Oxygen concentration and consumption within tissues and cells are critical parameters for metabolism and cell viability. The information gained from the measurement and imaging of the tissue oxygen can improve analysis and diagnosis of various diseases, such as neurological diseases and cancer [181–183]. An efficient method for the measurement of oxygen is based on oxygen-dependent quenching of metalloporphyrin phosphorescence. Platinum (Pt) and palladium (Pd) complex of porphyrin are suitable chromophores for oxygen dependent phosphorescence measurements due to their long lifetime and high quantum yield. Borisov et al. synthesized a series of Pt or Pd azatetrabenzoporphyrins (PtNTBP or PdNTBP) complex as oxygen indicators and PtNTBP showed spectral compatibility with 633 nm line of the He-Ne laser and the red laser diodes [184].

An optical PEBBLE (probes encapsulated by biologically localized embedding) nanosensors has been designed for dissolved oxygen in live cells [185]. Oxygen-sensitive Pt porphyrins, Pt(II) octaethylporphine and Pt(II) octaethylporphine ketone, were used as the indicator and

incorporated in ormosil nanoparticles 120 nm in size. Oxygen-insensitive dyes, 3,3′-dioctadecyloxacarbocyanine perchlorate and octaethylporphine, were chosen as reference dyes respectively. The oxygen-indicators and reference dyes were entrapped during the formation process of the ormosil particles via a sol-gel-based process. The Pt-porphyrin PEBBLE nanosensor showed 97% overall quenching response over the whole range of dissolved oxygen concentrations (0–43 ppm, saturated) indicating excellent sensitivity to the oxygen. In additional, the PEBBLE nanosensor exhibited a good reversibility and complete recovery at each time the environment changed between saturated N_2 to saturated O_2. The PEBBLE nanosensors were delivered to rat C6 glioma cells by gene gun and successfully achieved real-time measurement of the intracellular dissolved oxygen concentration.

Methodologies have been developed for assessment of local oxygen gradients via a panel of oxygen-sensitive probes. Three phosphorescent Pt-porphyrin probes targeted to the cell membrane(Per-NP) [186], MitoXpress [187] and Nano2 probes [188], were developed to monitor the pericellular (PC), extracellular (EC), and intracellular (IC) O_2 concentrations, respectively. MitoXpress was based on Pt(II)-coproporphyrin coupled albumin, Per-NP and Nano2 probes were Eudragit RL-100 based nanoparticles loaded with Pt(II)-tetrakis(pentafluorophenyl)porphyrin (PtPFPP) (Fig. 25A). Per-NP probes contained ER9Q-PtCP, a recombinant fluorescent protein that could target the cell membrane, to measure the PC oxygen. The Nano2 probes (Fig. 25B) showed cell-penetration due to the interaction between positive charge on the RL-100 nanoparticle surface and the cell membrane which is negatively charged outside. These three Pt-porphyrin and phosphorescence lifetime-based oxygen probes showed sensitive and accurate measurement for the EC, PC and IC O_2 in different cell models (Fig. 25C). In addition, the magnitude of the measurement could be modulated by changing cell density or adjusting the specific activity of the cells. This panel of oxygen probes proved a simple and minimally invasive methodology for the investigate oxygen gradients in tissue culture.

To image the intracellular oxygen in 3D with submicron spatial resolution, Brinas et al. reported the design of a nanosensor for oxygen by combining phosphorescence quenching and two-photon absorption (2PA) [189]. Via intramolecular energy transfer (ET), the 2PA antenna induced phosphorescence of the metalloporphyrin and the signal was amplified. Oxygen-sensitive Pt-porphyrin was selected as the central phosphorescent indicator due to the strong triplet state emission. The construct of the coupled Pt-porphyrin and 2PA antenna chromophores was entrapped in shielding dendrimers where the chromophores were packed in a high density resulting in a more effective molecular 2PA cross-section. To achieve the proposed design, several Pt porphyrin-coumarin based oxygen sensors were synthesized and analyzed. The results demonstrated the feasibility of the oxygen measurements by combining two-photon microscopy and Pt-porphyrin based phosphorescent dyes.

Based on the Nano2 intracellular oxygen (icO_2) probes, the Papkovsky group designed multimodal icO_2 probes (MM series) allowing for ratiometric or multi-photon imaging of icO_2 [190]. MM probes were composed of an O_2 sensitive phosphor, PtPFPP; an O_2-insensitive reference fluorophore as an antennae and FRET donor for PtTFPP, and the coating matrix cationic polymer RL-100 that formed the nanoparticle carrier for the encapsulation and delivery. For the reference antennae, the hydrophobic polymeric

fluorophore, PFO showed better performance than C545T which leaked out from the nanoparticles during cell loading and internalization. The O_2 calibration for MM2 probe loaded in MEF cells showed a lifetime range from 28 to 61 μs (Fig. 26A). MM2 probes could provide for high resolution imaging of the cellular O_2 based on ratiometric intensities and phosphorescence lifetime-based sensing under one- and two-photon excitation (Fig. 26B).

4. Conclusions

Metalloporphyrins are keys to fundamental bioprocesses required for life on earth. Increasingly, metalloporphyrins are being assessed for applications in biomedical fields. They are inherently suited for applications in theranostics due to their behavior as photoactive compounds for phototherapies and their utility for imaging with MRI, PET and optical modalities.

The central metals in the metalloporphyrins can enable axial coordination for other ligands, extending the diversity of metalloporphyrin nanomaterials. Metalloporphyrin nanoparticles could be modified with various functional groups via axial coordination following nanoparticle formation. Likewise, porphyrin nanoparticles could be modified with various metals following nanoparticle formation to impart diverse functions from a single batch of nanoparticles.

Much work remains to better understand and characterize both existing and new modular functions for metalloporphyrin nanoparticles. Likewise, more compelling applications need to be demonstrated. However, it is clear that porphyrin nanoparticles represent a promising platform for developing theranostic functions and metal chelation is central to these functions.

Acknowledgments

This work was supported by the National Institutes of Health (R01EB017270, DP5OD017898), the National Science Foundation (1555220) and the Government of India UGC-Raman Fellowship (5-104/2016 IC).

Abbreviations

AuNP	Gold nanoparticle
Dox	Doxorubicin
EPR	Enhanced Permeability and Retention
MRI	Magnetic resonance imaging
PDT	Photodynamic Therapy
PEG	Polyethylene glycol
PET	Positron emission tomography
PS	Photosensitizer

ROS	Reactive oxygen species
SERS	Surface enhance Raman scattering
SOD	Superoxide dismutase
UCL	Upconversion luminescence
UCNP	Upconversion nanoparticles

References

1. Zhang Y, Lovell JF. Theranostics. 22012; :905–915. [PubMed: 23082102]
2. Huang H, Song W, Rieffel J, Lovell JF. Frontiers in Physics. 32015;
3. Zhang Y, Lovell JF. Wiley Interdisciplinary Reviews: Nanomedicine and Nanobiotechnology. 92017; :e1420.
4. Josefsen LB, Boyle RW. Theranostics. 22012; :916–966. [PubMed: 23082103]
5. Zhou Y, Liang X, Dai Z. Nanoscale. 82016; :12394–12405. [PubMed: 26730838]
6. Klingenberg M. Arch Biochem Biophys. 751958; :376–386. [PubMed: 13534720]
7. Omura T. J Biol Chem. 2391964; :2370–2378. [PubMed: 14209971]
8. Lu AY, Coon MJ. J Biol Chem. 2431968; :1331–1332. [PubMed: 4385007]
9. Poulos TL. Chem Rev. 1142014; :3919. [PubMed: 24400737]
10. Baker NR. Annu Rev Plant Biol. 592008; :89–113. [PubMed: 18444897]
11. Melis A. Plant Sci. 1772009; :272–280.
12. Wu C, Niu Z, Tang Q, Huang W. Agricultural and forest meteorology. 1482008; :1230–1241.
13. Henson SA, Sarmiento JL, Dunne JP, Bopp L, Lima ID, Doney SC, John JG. C Beaulieu. 2010
14. Dror DK, Allen LH. Nutr Rev. 662008; :250–255. [PubMed: 18454811]
15. Yajnik C, Deshpande S, Jackson A, Refsum H, Rao S, Fisher D, Bhat D, Naik S, Coyaji K, Joglekar C. Diabetologia. 512008; :29–38. [PubMed: 17851649]
16. Allen LH. Am J Clin Nutrition. 892009; :693S–696S. [PubMed: 19116323]
17. RHU. Eur J Gen Med. 122015;
18. Thauer RK, Kaster AK, Seedorf H, Buckel W, Hedderich R. Nat Rev Microbiol. 62008; :579–591. [PubMed: 18587410]
19. Zheng K, Ngo PD, Owens VL, Yang X-p, Mansoorabadi SO. Science. 3542016; :339–342. [PubMed: 27846569]
20. Willner I, Willner B. Nano Lett. 102010; :3805–3815. [PubMed: 20843088]
21. Subbiah R, Veerapandian M, Yun KS. Curr Med Chem. 172010; :4559–4577. [PubMed: 21062250]
22. Sapsford KE, Algar WR, Berti L, Gemmill KB, Casey BJ, Oh E, Stewart MH, Medintz IL. Chem Rev. 1132013; :1904–2074. [PubMed: 23432378]
23. Huang H, Lovell JF. Adv Funct Mater. 272017; :1603524. [PubMed: 28824357]
24. Couvreur P. Adv Drug Del Rev. 652013; :21–23.
25. Luo D, Carter KA, Lovell JF. Wiley Interdisciplinary Reviews: Nanomedicine and Nanobiotechnology. 72015; :169–188. [PubMed: 25377691]
26. Acharya S, Sahoo SK. Adv Drug Del Rev. 632011; :170–183.
27. Torchilin V. Adv Drug Del Rev. 632011; :131–135.
28. Fang J, Nakamura H, Maeda H. Adv Drug Del Rev. 632011; :136–151.
29. Maeda H, Nakamura H, Fang J. Adv Drug Del Rev. 652013; :71–79.
30. Mura S, Nicolas J, Couvreur P. Nat Mat. 122013; :991–1003.
31. Pattni BS, Chupin VV, Torchilin VP. Chem Rev. 1152015; :10938–10966. [PubMed: 26010257]

32. Cheng R, Meng F, Deng C, Klok HA, Zhong Z. Biomaterials. 342013; :3647–3657. [PubMed: 23415642]
33. Kreuter J. Adv Drug Del Rev. 712014; :2–14.
34. Sapsford KE, Tyner KM, Dair BJ, Deschamps JR, Medintz IL. Anal Chem. 832011; :4453–4488. [PubMed: 21545140]
35. Kadish, KM, Smith, KM, Guilard, R. Porphyrin Handbook: Inorganic, organometallic and coordination chemistry. Elsevier; 2000. The
36. Kadish KM, Smith KM, Guilard R. World Scientific: Singapore. 20142010; :1–35.
37. Figge FH, Weiland GS, Manganiello LO. Proc Soc Exp Biol Med. 681948; :640–641. [PubMed: 18884315]
38. Waghorn PA. J Labelled Comp Radiopharm. 572014; :304–309. [PubMed: 24353174]
39. Smith, KM. Porphyrins and metalloporphyrins. Elsevier; Amsterdam: 1975.
40. Williams R. Chem Rev. 561956; :299–328.
41. Cuesta L, Sessler JL. Chem Soc Rev. 382009; :2716–2729. [PubMed: 19690749]
42. Scheidt WR. Acc Chem Res. 101977; :339–345.
43. Fleischer EB. Acc Chem Res. 31970; :105–112.
44. Dolphin, D. The Porphyrins. Vol. 1. Academic Press; New York: 1979.
45. Brothers PJ. J Porphyrins Phthalocyanines. 62002; :259–267.
46. Gong X, Milic T, Xu C, Batteas JD, Drain CM. J Am Chem Soc. 1242002; :14290–14291. [PubMed: 12452687]
47. Drain CM, Smeureanu G, Patel S, Gong X, Garno J, Arijeloye J. New J Chem. 302006; :1834–1843.
48. Xu LQ, Chen JC, Qian SS, Zhang AK, Fu GD, Li CM, Kang ET. Macromol Chem Phys. 2162015; :417–426.
49. Poursaberi T, Hassanisadi M, Torkestani K, Zare M. Chem Eng J. 1892012; :117–125.
50. Liang X, Li X, Jing L, Yue X, Dai Z. Biomaterials. 352014; :6379–6388. [PubMed: 24818886]
51. Yao X, Chen L, Chen X, Xie Z, Ding J, He C, Zhang J, Chen X. Acta Biomater. 252015; :162–171. [PubMed: 26190797]
52. Ince M, Hausmann A, Martínez-Díaz MV, Guldi DM, Torres T. Chem Commun. 482012; :4058–4060.
53. Mamaeva V, Sahlgren C, Lindén M. Adv Drug Del Rev. 652013; :689–702.
54. Huynh E, Zheng G. Nano Today. 92014; :212–222.
55. Lovell JF, Jin CS, Huynh E, Jin H, Kim C, Rubinstein JL, Chan WC, Cao W, Wang LV, Zheng G. Nat Mater. 102011; :324–332. [PubMed: 21423187]
56. Lovell JF, Jin CS, Huynh E, MacDonald TD, Cao W, Zheng G. Angew Chem Int Ed. 512012; : 2429–2433.
57. Li WS, Aida T. Chem Rev. 1092009; :6047–6076. [PubMed: 19769361]
58. Nishiyama N, Jang WD, Kataoka K. New J Chem. 312007; :1074–1082.
59. Hinshaw W, Bottomley PA, Holland G. Nature. 2701977; :722–723. [PubMed: 593393]
60. Aschner M, Guilarte TR, Schneider JS, Zheng W. Toxicol Appl Pharmacol. 2212007; :131–147. [PubMed: 17466353]
61. Todd DJ, Kay J. Annu Rev Med. 672016; :273–291. [PubMed: 26768242]
62. Punnagai M, Sateesh B, Sastry GN. ARKIVOC. 32005; :258–283.
63. Tulinsky A, Chen BM. J Am Chem Soc. 991977; :3647–3651. [PubMed: 858872]
64. Caravan P, Ellison JJ, McMurry TJ, Lauffer RB. Chem Rev. 991999; :2293–2352. [PubMed: 11749483]
65. Calvete MJF, Pinto SMA, Pereira MM, Geraldes CFGC. Coord Chem Rev. 3332017; :82–107.
66. Aime S, Botta M, Gianolio E, Terreno E. Angew Chem. 1122000; :763–766.
67. Takehara Y, Sakahara H, Masunaga H, Isogai S, Kodaira N, Sugiyama M, Takeda H, Saga T, Nakajima S, Sakata I. Magn Reson Med. 472002; :549–553. [PubMed: 11870842]

68. Zhang, X-a; Lovejoy, KS; Jasanoff, A; Lippard, SJ. Proc Nat Acad Sci. 1042007; :10780–10785. [PubMed: 17578918]
69. Zhang Z, He R, Yan K, Guo Q-n, Lu Y-g, Wang X-x, Lei H, Li Z-y. Bioorg Med Chem Lett. 192009; :6675–6678. [PubMed: 19850475]
70. Pan D, Caruthers SD, Hu G, Senpan A, Scott MJ, Gaffney PJ, Wickline SA, Lanza GM. J Am Chem Soc. 1302008; :9186–9187. [PubMed: 18572935]
71. Jing L, Liang X, Li X, Yang Y, Dai Z. Acta Biomater. 92013; :9434–9441. [PubMed: 23962645]
72. Jing L, Liang X, Li X, Lin L, Yang Y, Yue X, Dai Z. Theranostics. 42014; :858. [PubMed: 25057312]
73. Zou T, Zhen M, Chen D, Li R, Guan M, Shu C, Han H, Wang C. Dalton Transactions. 442015; : 9114–9119. [PubMed: 25899301]
74. MacDonald TD, Liu TW, Zheng G. Angew Chem Int Ed. 532014; :6956–6959.
75. Keca JM, Chen J, Overchuk M, Muhanna N, MacLaughlin CM, Jin CS, Foltz WD, Irish JC, Zheng G. Angew Chem. 1282016; :6295–6299.
76. Shao S, Do TN, Razi A, Chitgupi U, Geng J, Alsop RJ, Dzikovski BG, Rheinstädter MC, Ortega J, Karttunen M. Small. 132017;
77. Ethirajan M, Chen Y, Joshi P, Pandey RK. Chem Soc Rev. 402011; :340–362. [PubMed: 20694259]
78. Carter KA, Shao S, Hoopes MI, Luo D, Ahsan B, Grigoryants VM, Song W, Huang H, Zhang G, Pandey RK. Nat Commun. 52014; :3546. [PubMed: 24699423]
79. Carter KA, Luo D, Razi A, Geng J, Shao S, Ortega J, Lovell JF. Theranostics. 62016; :2329. [PubMed: 27877238]
80. Kress J, Rohrbach DJ, Carter KA, Luo D, Shao S, Lele S, Lovell JF, Sunar U. Biomed Opt Express. 62015; :3546–3555. [PubMed: 26417522]
81. Luo D, Carter KA, Razi A, Geng J, Shao S, Giraldo D, Sunar U, Ortega J, Lovell JF. Biomaterials. 752016; :193–202. [PubMed: 26513413]
82. Luo D, Carter KA, Razi A, Geng J, Shao S, Lin C, Ortega J, Lovell JF. J Control Release. 2202015; :484–494. [PubMed: 26578438]
83. Luo D, Li N, Carter KA, Lin C, Geng J, Shao S, Huang WC, Qin Y, Atilla-Gokcumen GE, Lovell JF. Small. 122016; :3039–3047. [PubMed: 27121003]
84. Sunar U, Kress J, Rohrbach DJ, Carter K, Luo D, Shao S, Lele S, Lovell JF. Cancer Imaging Ther. 2016:JW4A.
85. Jahanbin T, Sauriat-Dorizon H, Spearman P, Benderbous S, Korri-Youssoufi H. Mat Sci Eng C. 522015; :325–332.
86. Gong H, Dong Z, Liu Y, Yin S, Cheng L, Xi W, Xiang J, Liu K, Li Y, Liu Z. Adv Funct Mater. 242014; :6492–6502.
87. Rieffel J, Chitgupi U, Lovell JF. Small. 112015; :4445–4461. [PubMed: 26185099]
88. Lee DE, Koo H, Sun IC, Ryu JH, Kim K, Kwon IC. Chem Soc Rev. 412012; :2656–2672. [PubMed: 22189429]
89. Liang X, Li Y, Li X, Jing L, Deng Z, Yue X, Li C, Dai Z. Adv Funct Mater. 252015; :1451–1462.
90. Young SW, Sidhu MK, Qing F, Muller HH, Neuder M, Zanassi G, Mody TD, Hemmi G, Dow W, Mutch JD, Sessler JL, Miller RA. Invest Radiol. 291994; :330–338. [PubMed: 8175308]
91. Young SW, Qing F, Harriman A, Sessler JL, Dow WC, Mody TD, Hemmi GW, Hao Y, Miller RA. Proc Nat Acad Sci. 931996; :6610–6615. [PubMed: 8692865]
92. Sessler JL, Mody TD, Hemmi GW, Lynch V, Young SW, Miller RA. J Am Chem Soc. 1151993; : 10368–10369.
93. Barkey NM, Preihs C, Cornnell HH, Martinez G, Carie A, Vagner J, Xu L, Lloyd MC, Lynch VM, Hruby VJ. J Med Chem. 562013; :6330–6338. [PubMed: 23863078]
94. Lee MH, Kim EJ, Lee H, Kim HM, Chang MJ, Park SY, Hong KS, Kim JS, Sessler JL. J Am Chem Soc. 1382016; :16380–16387. [PubMed: 27998081]
95. Yoon HJ, Lim TG, Kim JH, Cho YM, Kim YS, Chung US, Kim JH, Choi BW, Koh WG, Jang WD. Biomacromol. 152014; :1382–1389.

96. Mbakidi JP, Brégier F, Ouk TS, Granet R, Alves S, Rivière E, Chevreux S, Lemercier G, Sol V. Chem Plus Chem. 802015; :1416–1426.

97. Boudon J, Paris J, Bernhard Y, Popova E, Decréau RA, Millot N. Chem Commun. 492013; :7394–7396.

98. Xuan, S-h; Lee, S-F; Lau, JT-F; Zhu, X; Wang, Y-XJ; Wang, F; Lai, JM; Sham, KW; Lo, P-C; Yu, JC. ACS applied Mater Interfaces. 42012; :2033–2040.

99. Townsend, DW, Beyer, T, Blodgett, TM. Semin Nucl Med. Elsevier; 2003. 193–204.

100. Elsinga PH. Nuclear Med Rev. 152012; :13–16.

101. Ali H, van Lier JE. Chem Rev. 991999; :2379–2450. [PubMed: 11749485]

102. Sadeghi S, Mirzaei M, Rahimi M, Jalilian AR. Asia Oceania J Nuclear Med Biol. 22014; :95–103.

103. Lee JH, Shao S, Cheng KT, Lovell JF, Paik CH. J Liposome Res. 252015; :101–106. [PubMed: 24963601]

104. Waghorn PA. J Labelled Compounds Radiopharm. 572014; :304–309.

105. Figge FH, Weiland GS, Manganiello LO. Proc Soc Exp Biol Med. 681948; :640–641. [PubMed: 18884315]

106. Srivatsan A, Missert JR, Upadhyay SK, Pandey RK. J Porphyrins Phthalocyanines. 192015; :109–134.

107. Wrenn FR, Good ML, Handler P. Science. 1131951; :525–527. [PubMed: 14828392]

108. Blower PJ, Lewis JS, Zweit J. Nucl Med Biol. 231996; :957–980. [PubMed: 9004284]

109. Jeeves, WP, Wilson, BC, Firnau, G, Brown, K. Methods in Porphyrin Photosensitization. Springer; 1985. Studies of HPD and radiolabelled HPD in-vivo and in-vitro; 51–67.

110. Wilson BC, Firnau G, Jeeves WP, Brown KL, Burns-McCormick DM. Lasers Med Sci. 31988; : 71–80.

111. Shi J, Liu T, Chen J, Green D, Jaffray D, Wilson BC, Wang F, Zheng G. Theranostics. 12011; : 363–370. [PubMed: 21938264]

112. Liu TW, MacDonald TD, Shi J, Wilson BC, Zheng G. Angew Chem Int Ed. 512012; :13128–13131.

113. Liu TW, MacDonald TD, Jin CS, Gold JM, Bristow RG, Wilson BC, Zheng G. ACS Nano. 72013; :4221–4232. [PubMed: 23544841]

114. Rieffel J, Chen F, Kim J, Chen G, Shao W, Shao S, Chitgupi U, Hernandez R, Graves SA, Nickles RJ. Adv Mater. 272015; :1785–1790. [PubMed: 25640213]

115. Huang H, Hernandez R, Geng J, Sun H, Song W, Chen F, Graves SA, Nickles RJ, Cheng C, Cai W. Biomaterials. 762016; :25–32. [PubMed: 26517562]

116. Zhang Y, Wang D, Goel S, Sun B, Chitgupi U, Geng J, Sun H, Barnhart TE, Cai W, Xia J. Adv Mater. 282016; :8524–8530. [PubMed: 27396479]

117. Zhang Y, Jeon M, Rich LJ, Hong H, Geng J, Zhang Y, Shi S, Barnhart TE, Alexandridis P, Huizinga JD, Seshadri M, Cai W, Kim C, Lovell JF. Nat Nanotechnol. 92014; :631–638. [PubMed: 24997526]

118. Li Y, Lin T-y, Luo Y, Liu Q, Xiao W, Guo W, Lac D, Zhang H, Feng C, Wachsmann-Hogiu S, Walton JH, Cherry SR, Rowland DJ, Kukis D, Pan C, Lam KS. Nat Commun. 52014;

119. Feng L, Cheng L, Dong Z, Tao D, Barnhart TE, Cai W, Chen M, Liu Z. ACS nano. 2016

120. Kneipp J, Kneipp H, Kneipp K. Chem Soc Rev. 372008; :1052–1060. [PubMed: 18443689]

121. Qian X, Peng XH, Ansari DO, Yin-Goen Q, Chen GZ, Shin DM, Yang L, Young AN, Wang MD, Nie S. Nat Biotechnol. 262008; :83–90. [PubMed: 18157119]

122. Hamer M, Rezzano IN. Inorg Chem. 552016; :8595–8602. [PubMed: 27482597]

123. Ferreira LM, Grasseschi D, Santos MS, Martins PR, Gutz IG, Ferreira AMC, Araki K, Toma HE, Angnes Lc. Langmuir. 312015; :4351–4360. [PubMed: 25812035]

124. Murphy S, Huang L, Kamat PV. J Phys Chem C. 1152011; :22761–22769.

125. Tam NC, Scott BM, Voicu D, Wilson BC, Zheng G. Bioconjug Chem. 212010; :2178–2182. [PubMed: 21090645]

126. Tam NC, McVeigh PZ, MacDonald TD, Farhadi A, Wilson BC, Zheng G. Bioconjug Chem. 232012; :1726–1730. [PubMed: 22876736]
127. Farhadi A, Roxin Á, Wilson BC, Zheng G. Theranostics. 52015; :469. [PubMed: 25767614]
128. Abuteen A, Zanganeh S, Akhigbe J, Samankumara LP, Aguirre A, Biswal N, Braune M, Vollertsen A, Röder B, Brückner C. Phys Chem Chem Phys. 152013; :18502–18509. [PubMed: 24071709]
129. Huynh E, Jin CS, Wilson BC, Zheng G. Bioconjug Chem. 252014; :796–801. [PubMed: 24621279]
130. Ng KK, Takada M, Harmatys K, Chen J, Zheng G. ACS Nano. 102016; :4092–4101. [PubMed: 27015124]
131. Yu M, Li F, Chen Z, Hu H, Zhan C, Yang H, Huang C. Anal Chem. 812009; :930–935. [PubMed: 19125565]
132. Yang T, Sun Y, Liu Q, Feng W, Yang P, Li F. Biomaterials. 332012; :3733–3742. [PubMed: 22361097]
133. Chen G, Shen J, Ohulchanskyy TY, Patel NJ, Kutikov A, Li Z, Song J, Pandey RK, Ågren H, Prasad PN. ACS Nano. 62012; :8280–8287. [PubMed: 22928629]
134. Singh-Rachford TN, Haefele A, Ziessel R, Castellano FN. J Am Chem Soc. 1302008; :16164–16165. [PubMed: 18998677]
135. Liu Q, Yang T, Feng W, Li F. J Am Chem Soc. 1342012; :5390–5397. [PubMed: 22369318]
136. Liu Q, Yin B, Yang T, Yang Y, Shen Z, Yao P, Li F. J Am Chem Soc. 1352013; :5029–5037. [PubMed: 23464990]
137. Hayyan M, Hashim MA, AlNashef IM. Chem Rev. 1162016; :3029–3085. [PubMed: 26875845]
138. Dolmans DE, Fukumura D, Jain RK. Nat Rev Cancer. 32003; :380–387. [PubMed: 12724736]
139. Brown SB, Brown EA, Walker I. Lancet Oncol. 52004; :497–508. [PubMed: 15288239]
140. Pansare VJ, Hejazi S, Faenza WJ, Prud'homme RK. Chem Mater. 242012; :812–827. [PubMed: 22919122]
141. Harriman A. Faraday Transactions 1. 761980; :1978–1985.
142. Lavis LD, Raines RT. ACS Chem Biol. 32008; :142–155. [PubMed: 18355003]
143. Nyokong T. Coord Chem Rev. 2512007; :1707–1722.
144. Harriman A. Journal of the Chemical Society, Faraday Transactions 2. 771981; :1281–1291.
145. Carter KA, Wang S, Geng J, Luo D, Shao S, Lovell JF. Mol Pharm. 132015; :420–427. [PubMed: 26691879]
146. Ricci-Júnior E, Marchetti JM. Int J Pharm. 3102006; :187–195. [PubMed: 16442755]
147. Yao X, Chen X, He C, Chen L, Chen X. J Mater Chem B. 32015; :4707–4714.
148. Luo D, Carter KA, Miranda D, Lovell JF. Advanced Science. 42017; :1600106. [PubMed: 28105389]
149. Sekkat N, Bergh Hvd, Nyokong T, Lange N. Molecules. 172012; :98.
150. Muehlmann LA, Ma BC, Longo JPF, Santos MdFMA, Azevedo RB. Int J Nanomed. 92014; : 1199.
151. Zhang P, Steelant W, Kumar M, Scholfield M. J Am Chem Soc. 1292007; :4526–4527. [PubMed: 17385866]
152. Wang F, Chen X, Zhao Z, Tang S, Huang X, Lin C, Cai C, Zheng N. J Mater Chem. 212011; : 11244–11252.
153. Zhao Z, Han Y, Lin C, Hu D, Wang F, Chen X, Chen Z, Zheng N. Chem Asian J. 72012; :830–837. [PubMed: 22279027]
154. Cui S, Yin D, Chen Y, Di Y, Chen H, Ma Y, Achilefu S, Gu Y. ACS Nano. 72012; :676–688. [PubMed: 23252747]
155. Lau JT, Lo PC, Jiang XJ, Wang Q, Ng DK. J Med Chem. 572014; :4088–4097. [PubMed: 24793456]
156. Shao S, Geng J, Yi HA, Gogia S, Neelamegham S, Jacobs A, Lovell JF. Nat Chem. 72015; :438–46. [PubMed: 25901823]

157. Li Y, Hill A, Beitelshees M, Shao S, Lovell JF, Davidson BA, Knight PR, Hakansson AP, Pfeifer BA, Jones CH. Proc Nat Acad Sci. 1132016; :6898–6903. [PubMed: 27274071]
158. El-Khouly ME, Ito O, Smith PM, D'Souza F. J Photochem Photobiol C. 52004; :79–104.
159. Konarev DV, Khasanov SS, Lyubovskaya RN. Coord Chem Rev. 2622014; :16–36.
160. Lebedeva MA, Chamberlain TW, Khlobystov AN. Chem Rev. 1152015; :11301–11351. [PubMed: 26421732]
161. Ishii T, Aizawa N, Kanehama R, Yamashita M, Sugiura K-i, Miyasaka H. Coord Chem Rev. 2262002; :113–124.
162. Konarev DV, Khasanov SS, Otsuka A, Saito G, Lyubovskaya RN. Chem European J. 122006; : 5225–5230. [PubMed: 16671049]
163. Olmstead MM, Costa DA, Maitra K, Noll BC, Phillips SL, Van Calcar PM, Balch AL. J Am Chem Soc. 1211999; :7090–7097.
164. Boyd PD, Hodgson MC, Rickard CE, Oliver AG, Chaker L, Brothers PJ, Bolskar RD, Tham FS, Reed CA. J Am Chem Soc. 1211999; :10487–10495.
165. Konarev DV, Khasanov SS, Faraonov MA, Lyubovskaya RN. Cryst Eng Comm. 142012; :4350–4356.
166. Konarev DV, Khasanov SS, Otsuka A, Yoshida Y, Saito G. J Am Chem Soc. 1242002; :7648–7649. [PubMed: 12083905]
167. Konarev DV, Khasanov SS, Saito G, Lyubovskaya RN, Yoshida Y, Otsuka A. Chem European J. 92003; :3837–3848. [PubMed: 12916108]
168. Konarev DV, Khasanov SS, Otsuka A, Saito G, Lyubovskaya RN. Dalton Transactions. 2009:6416–6420. [PubMed: 19655076]
169. Konarev DV, Khasanov SS, Kornev AB, Faraonov MA, Troshin PA, Lyubovskaya RN. Dalton Transactions. 412012; :791–798. [PubMed: 22075578]
170. Song L-C, Liu X-F, Xie Z-J, Luo F-X, Song H-B. Inorg Chem. 502011; :11162–11172. [PubMed: 21999524]
171. Ohse T, Nagaoka S, Arakawa Y, Kawakami H, Nakamura K. J Inorg Biochem. 852001; :201–208. [PubMed: 11410240]
172. Kasugai N, Murase T, Ohse T, Nagaoka S, Kawakami H, Kubota S. J Inorg Biochem. 912002; : 349–355. [PubMed: 12161304]
173. Kawakami H, Hiraka K, Tamai M, Horiuchi A, Ogata A, Hatsugai T, Yamaguchi A, Oyaizu K, Yuasa M. Polym Adv Technol. 182007; :82–87.
174. Hiraka K, Kanehisa M, Tamai M, Asayama S, Nagaoka S, Oyaizu K, Yuasa M, Kawakami H. Colloids Surf B Biointerfaces. 672008; :54–58. [PubMed: 18775654]
175. Yuasa M, Oyaizu K, Horiuchi A, Ogata A, Hatsugai T, Yamaguchi A, Kawakami H. Mol Pharm. 12004; :387–389. [PubMed: 16026010]
176. Umakoshi H, Morimoto K, Ohama Y, Nagami H, Shimanouchi T, Kuboi R. Langmuir. 242008; : 4451–4455. [PubMed: 18366234]
177. Kanehisa M, Asayama S, Kawakami H. Desalination Water Treatment. 172010; :31–36.
178. Aikawa T, Ito S, Shinohara M, Kaneko M, Kondo T, Yuasa M. Biomaterials Sci. 32015; :861–869.
179. Lee H, Hong K-I, Jang W-D. Coord Chem Rev. 2017
180. Huang H, Chauhan S, Geng J, Qin Y, Watson DF, Lovell JF. Biomacromolecules. 182017; :562–567. [PubMed: 28146351]
181. Hagen T, Taylor CT, Lam F, Moncada S. Science. 3022003; :1975–1978. [PubMed: 14671307]
182. Abramov AY, Scorziello A, Duchen MR. J Neurosci. 272007; :1129–1138. [PubMed: 17267568]
183. Evans SM, Koch CJ. Cancer Lett. 1952003; :1–16. [PubMed: 12767506]
184. Borisov SM, Zenkl G, Klimant I. ACS Applied Mater Interfaces. 22010; :366–374.
185. Koo YEL, Cao Y, Kopelman R, Koo SM, Brasuel M, Philbert MA. Anal Chem. 762004; :2498–2505. [PubMed: 15117189]
186. Dmitriev RI, Zhdanov AV, Jasionek G, Papkovsky DB. Anal Chem. 842012; :2930–2938. [PubMed: 22380020]

187. O'Riordan TC, Zhdanov AV, Ponomarev GV, Papkovsky DB. Anal Chem. 792007; :9414–9419. [PubMed: 18001129]

188. Fercher A, Borisov SM, Zhdanov AV, Klimant I, Papkovsky DB. ACS Nano. 52011; :5499–5508. [PubMed: 21671589]

189. Briñas RP, Troxler T, Hochstrasser RM, Vinogradov SA. J Am Chem Soc. 1272005; :11851. [PubMed: 16104764]

190. Kondrashina AV, Dmitriev RI, Borisov SM, Klimant I, O'Brien I, Nolan YM, Zhdanov AV, Papkovsky DB. Adv Funct Mater. 222012; :4931–4939.

Highlights

- Metalloporphyrin nanoparticles have been described for a range of bio-applications
- Metal-chelation can functionalize porphyrin nanoparticles in a modular way
- Metal chelation can occur before or after nanoparticle formation
- Specific metals confer unique sensing, imaging and therapy attributes
- Specific metals confer capacity for axial coordination and functionalization

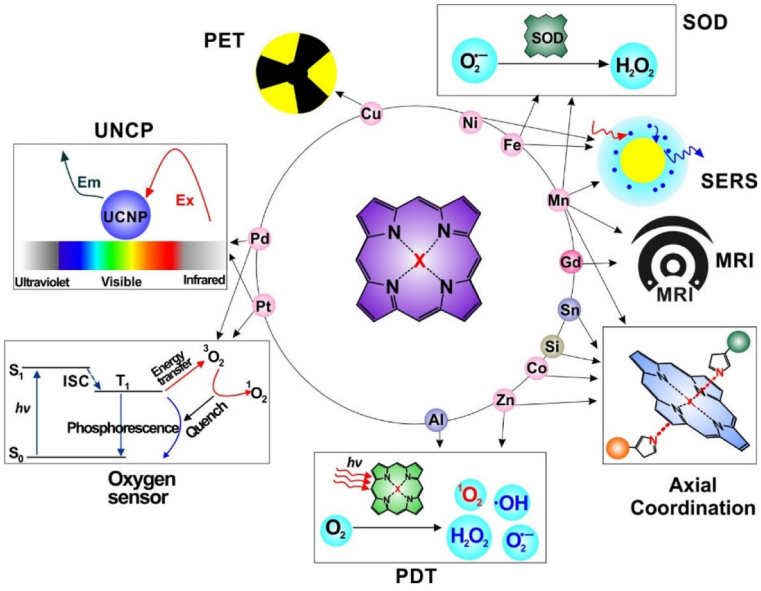

Figure 1.

Illustrative biomedical applications of porphyrins enabled via the coordination of different metals in the core of the macrocycle.

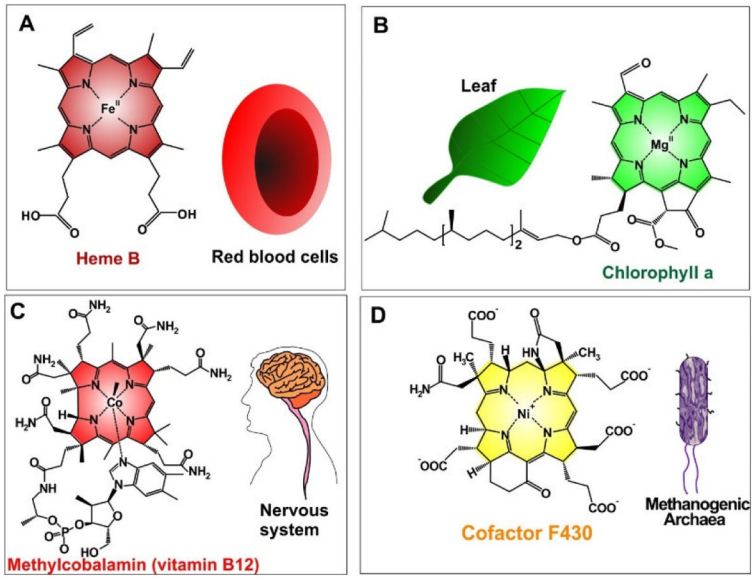

Figure 2.

Examples of natural metalloporphyrins. A) Heme B, an iron(II)-porphyrin compound in red blood cells, participates in the transportation of oxygen. B) ChlorophyII a, a magnesium chlorin, plays crucial role in the photosynthesis. C) Methylcobalamin (vitamin B12), a vitamin required for nervous system function. D) Cofactor F430 catalyzes methanogenesis in methanogenic archaea.

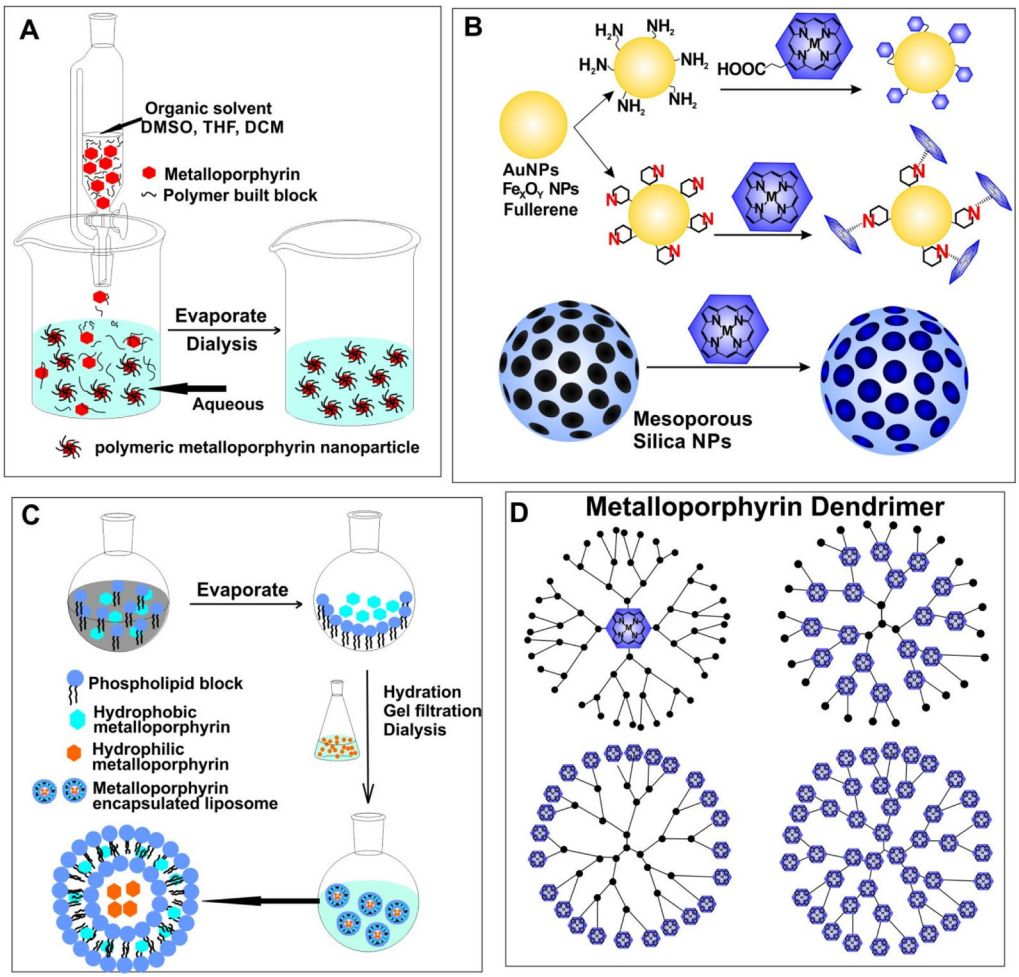

Figure 3.

Examples of metalloporphyrin nanoparticle preparation. A) Solvent mixing to form polymeric metalloporphyrin nanoparticles. B) Grafting metalloporphyrins to existing nanoparticle via either covalent binding or chelation. C) Liposomal formulation of metalloporphyrins; hydrophilic and hydrophobic metalloporphyrin are encapsulated in the liposome core or within the lipid bilayer, respectively. D) Structures of different types of metalloporphyrin dendrimers. Metalloporphyrins can occupy the cores, branch nodes, terminal nodes or all nodes.

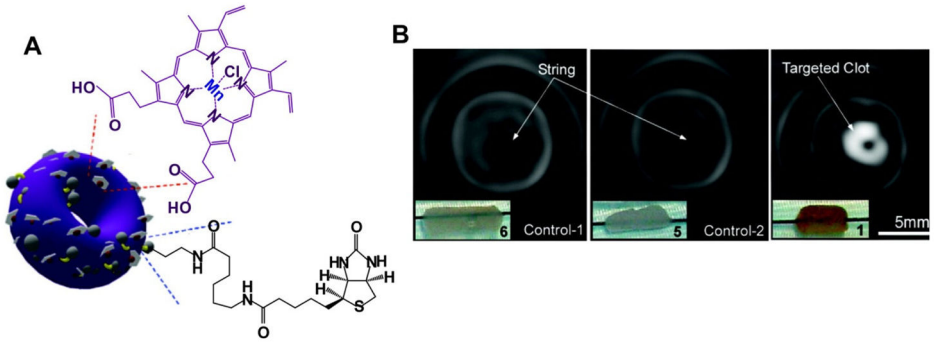

Figure 4.

Self-assembled nanobialys. A) The structure of Mn(III) porphyrin nanobialys. Mn(III) porphyrin provided MRI contrast. B) MRI of fibrin-targeted nanobialys (1) (right) or control group with biotin and no metal (6)(left), or no biotin with metal (5)(middle) bound to cylindrical plasma clots measured at 3.0 T. Permission obtained from Ref.[70]. Copyright (2008) by the American Chemical Society.

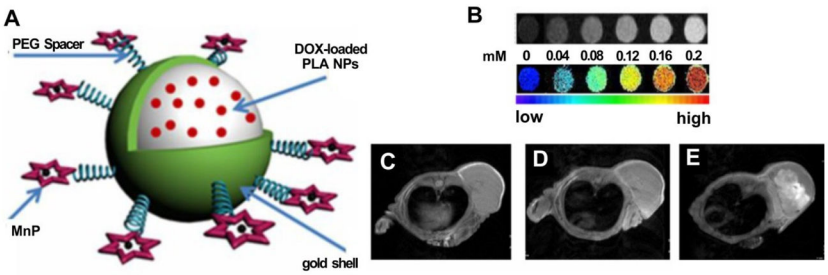

Figure 5.

Mn-porphyrin, PLA-coated Au nanoshells. A) DOX@PLA@Au-PEG-MnP NPs. Mn-porphyrin was grafted on the surface for MRI contrast. B) T1-weighted images of DOX@PLA@Au-PEG-MnP NPs at different concentrations at 0.5 T, 37 °C. In vivo T1-weighted images before injection (C), 0.5h (D) and 24h (E) post-injection of nanoparticles. Permission obtained from Ref.[72]. Copyright (2014) by Ivyspring.

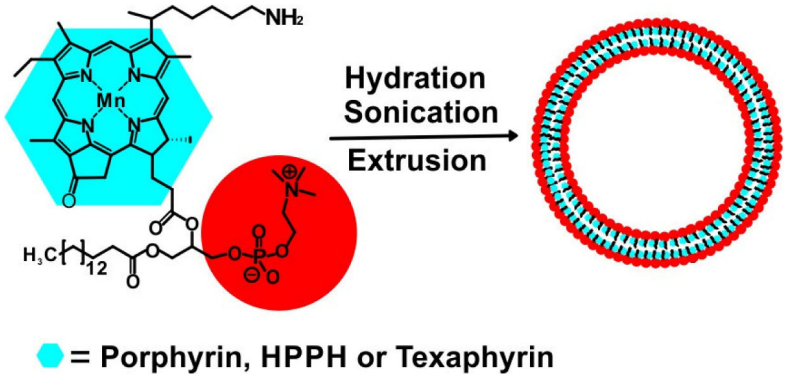

Figure 6.

The structure of a sample Mn-porphyrin-phospholipid and assembled Mn-porphyrin liposome such as Mn-porphyrin-liposomes [74], Mn-nanotexaphyrin [75], Mn-HPPH liposome and Mn-N-HPPH liposomes [76]. The Mn-porphyrin is conjugated to the side chain of a lysophospholipid and the obtained Mn-porphyrin-lipid self-assembles in a bilayer structure.

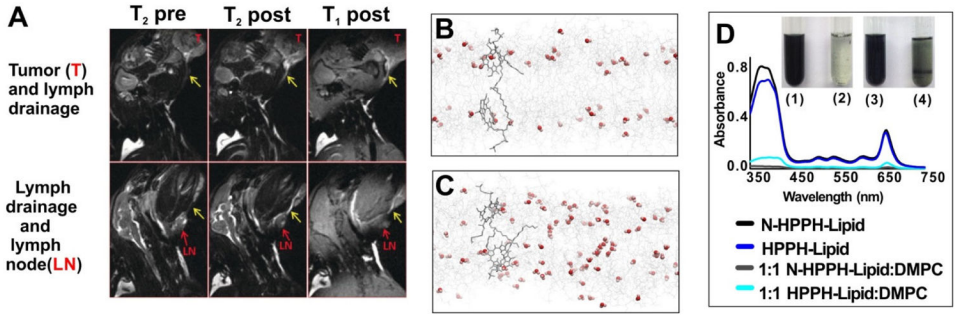

Figure 7.

A) In vivo MRI imaging of tumor (top) and lymph node (bottom) in mice administrated with Mn-nanotexaphyrin (8 mg mL^{-1}, 1.5 mL). Molecular dynamics simulations of HPPH-lipid (B) and N-HPPH-lipid (C) bilayer. Water molecules are shown as red spheres and lipids as gray wires. D) Optical absorption and inset photo of hydrated lipid film of different formulations. N-HPPH-lipid, but not the HPPH-lipid formed a dark solution without aggregation after water addition and shaking. Permission obtained from Ref.[75] and [76]. Copyright by Wiley.

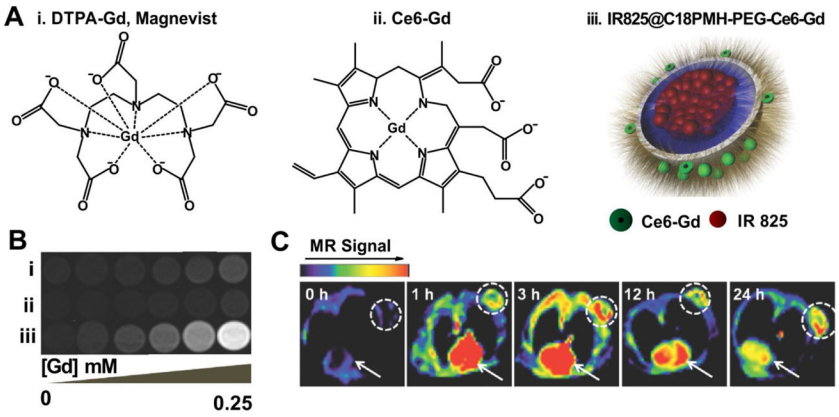

Figure 8.

Multifunctional polymeric nanomicelles. A) The structure of (i) DTPA-Gd, (ii) Ce6-Gd and (iii) IR825@18PMH-PEG-Ce6-Gd. B) The T1-weighted MR images of three different contrasts at different Gd concentration. C) In vivo MR imaging of 4T1 tumor-bearing mice administrated IR825@C18PMH-PEG-Ce6-Gd. Dashed circle highlighted the tumor site and the arrows pointed out the heart area. Permission obtained from Ref.[86]. Copyright (2014) by Wiley.

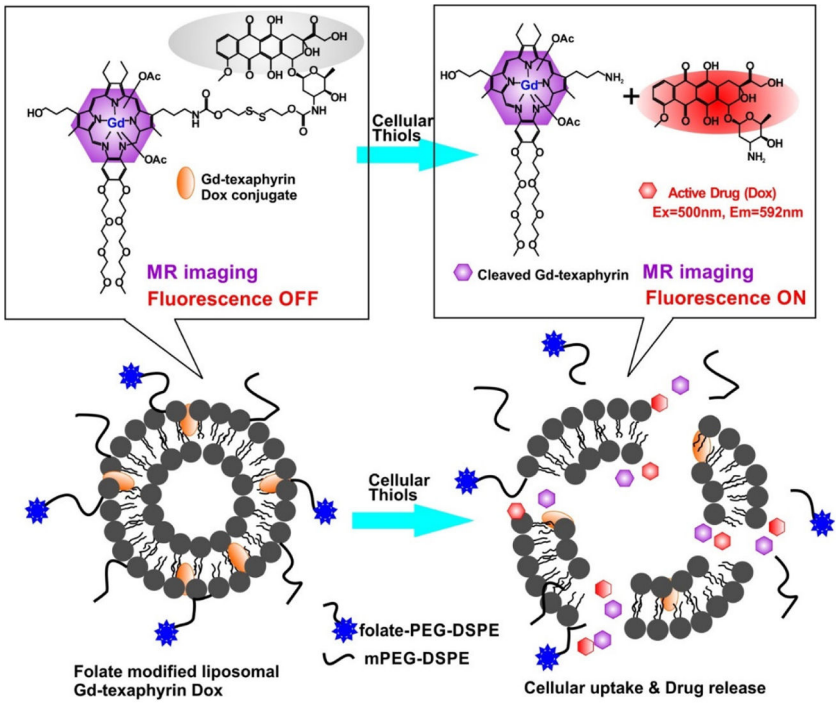

Figure 9.

Folate-receptor-targeted liposomal Gd-texaphyrin conjugated doxorubicin. The cleavage of the bond between Gd-texaphyrin and doxorubicin resulted in the restoring fluorescence of doxorubicin. Permission obtained from Ref.[94]. Copyright (2016) by American Chemical Society.

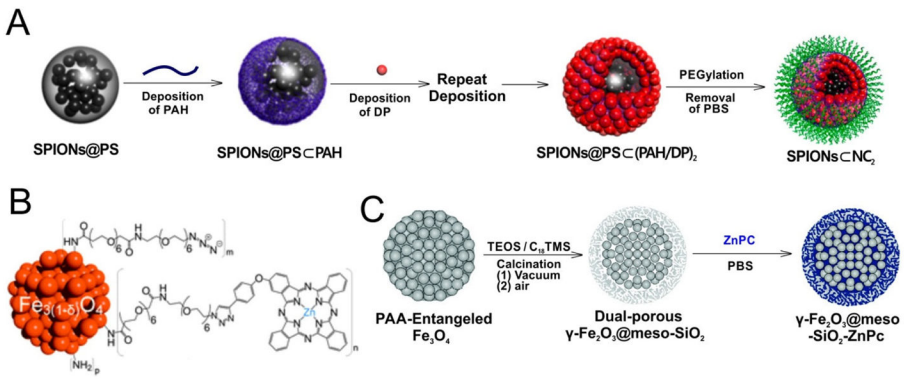

Figure 10.

Preparation and structure of different T2-weighted metalloporphyrin nanoparticles. A) Layer-by layer self-assembled fabrication of SPIONs nanocapsule. B) The structure of SPION grafted by ZnPC. C) Schematic for the preparation of γ-Fe_2O_3@*meso*-SiO_2–ZnPC. Permission obtained from Ref.[95, 97, 98]. Copyright by American Chemical Society, Royal Society of Chemistry.

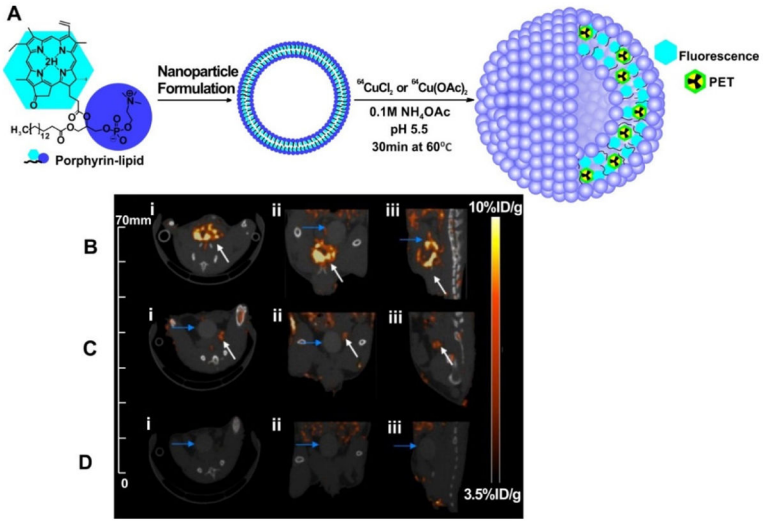

Figure 11.

^{64}Cu-porphysomes as a PET agent. A) Schematic diagram of the multimodal properties of ^{64}Cu-porphysomes as a result of directly radiolabeling a fraction of the porphyrin-lipid bilayer of preformed photonic porphysomes creating intrinsic multimodal nanoparticles. ^{64}Cu-porphysome selectivity in orthotopic prostate tumor models. Representative MicroPET/CT images of (i) axial, (ii) coronal, and (iii) sagittal single slices through (B) orthotopic PC3 tumor (n = 8), (C) orthotopic 22RV1 tumor (n = 3), and (D) healthy male mice (n = 3) at 24 h after intravenous injection of 500μL Ci ^{64}Cu-porphysomes: PET image integration time 40 min. White arrows depict prostate tumor; blue arrows depict bladder. Permission obtained from Ref.[113]. Copyright (2013) by American Chemical Society.

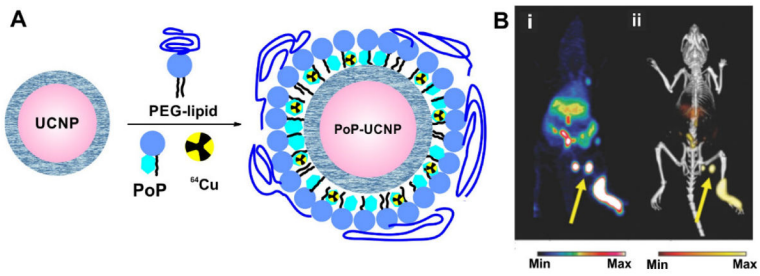

Figure 12.

^{64}Cu-PoP coated UCNPs as multifunctional imaging agent. A) Schematic diagram of the PoP-UCNP structure. Core-shell UCNPs were transferred to the aqueous phase by lipid coating with PEG-lipid and PoP. Radioactive ^{64}Cu can seamlessly chelate inside. B) Accumulation of PoP-UCNPs in the first draining lymph node is indicated with yellow arrows in full anatomy PET (left), merged PET/CT (right). Permission obtained from Ref. [114]. Copyright (2015) by Wiley.

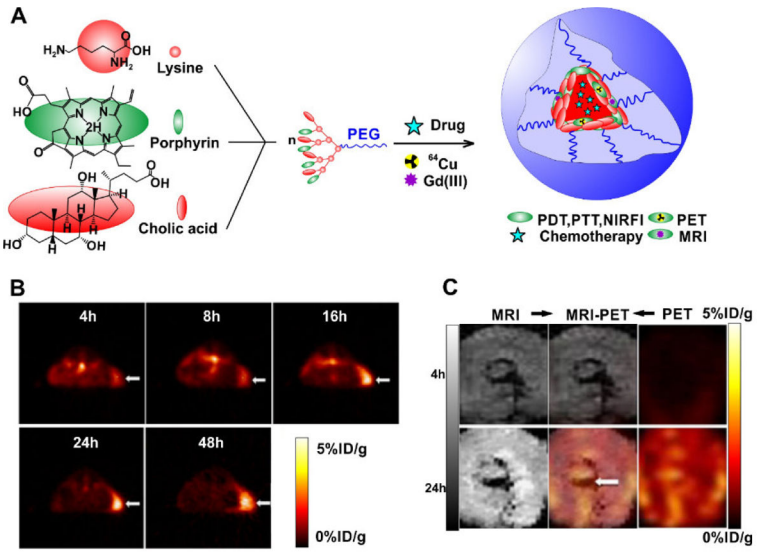

Figure 13.

Self-assembled multifunctional nanoporphyrin. A) Schematic illustration of a multifunctional NP self-assembled by a representative porphyrin–telodendrimer, PEG5k-Por4-CA4, composed of four pyropheophorbide-a molecules and four cholic acids attached to the terminal end of a linear PEG chain. B) PET image of nude mice bearing SKOV3 ovarian cancer xenografts at 4, 8, 16, 24 and 48 h post injection of ^{64}Cu-labelled NPs (150–200 ml, ^{64}Cu dose: 0.6–0.8 mCi). The white arrow points to the tumor site. C) PET-MR images of tumor slices of nude mice bearing A549 lung cancer xenograft at 4 or 24 h post injection of dual-labelled NPs. White arrow points to the necrotic area in the center of the tumor. Permission obtained from Ref.[118]. Copyright (2014) by Springer Nature.

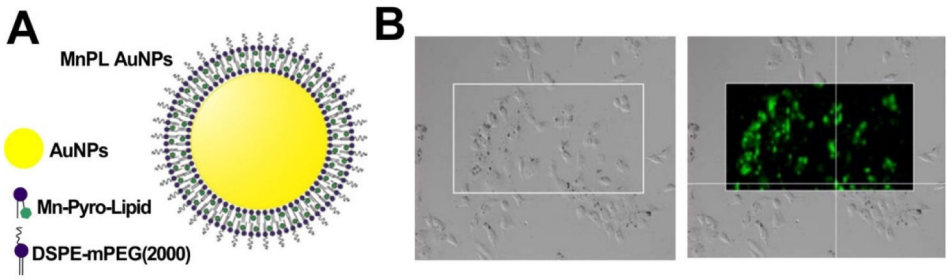

Figure 14.

Porphyrin-lipid coated gold nanoparticles as SERS agents. A) The structure of MnPL AuNPs. The Mn-porphyrin lipid was served as both the SERS dye and the biocompatible surface coating. B) The microscopy images of A549 lung cancer cells showing MnPL AuNP used for cellular imaging. Permission obtained from Ref.[126]. Copyright (2012) by American Chemical Society.

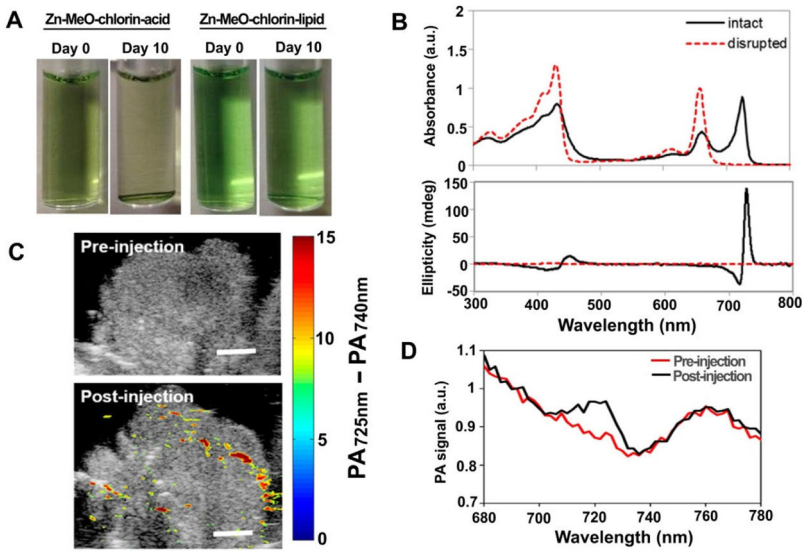

Figure 15.

Zn-MeO-porphyrin lipid nanovesicles for PA contrast agent. A) Photographs of Zn-MeO-chlorin acid (20%) and Zn-MeO-chlorin lipid (20%) after storage at room temperature for 10 days. Precipitation was observed in the Zn-MeO-chlorin acid sample after 10 days of storage. B) UV–vis absorption and CD spectra for 20% Zn-MeO-chlorin lipid. C) PA image of hamster cheek pouch tumor pre-injection and 5 min post-injection of the Zn-MeO-chlorin lipid nanovesicle. D) Quantitative analysis of the PA signal in the tumor site pre-injection and 5 min post-injection of the Zn-MeO-chlorin lipid nanovesicle. Permission obtained from Ref.[130]. Copyright (2016) by American Chemical Society.

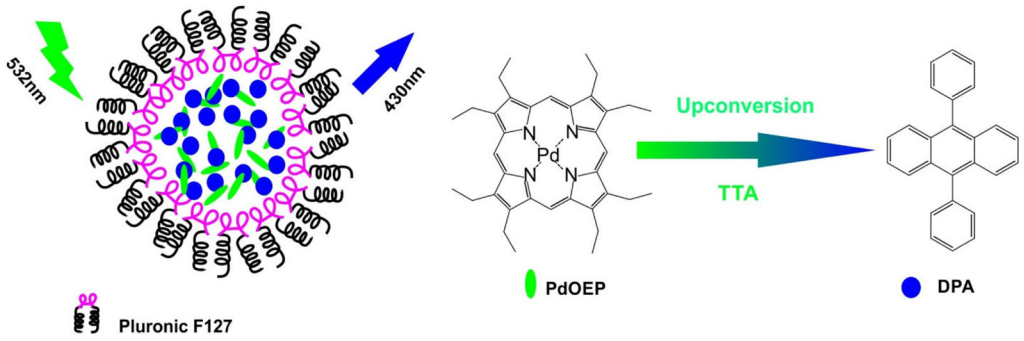

Figure 16.

TAA-UCNP co-loaded with PdOEP and DPA. Schematic illustration of TAA-UCNP, the chemical structure of PdOEP (sensitizer) and DPA (annihilator). The chelation of palladium (Pd) enhanced the phosphorescence of porphyrin molecules and thus it has the potential to be used as a triplet photosensitizer for upconversion. Permission obtained from Ref.[135]. Copyright (2012) by American Chemical Society.

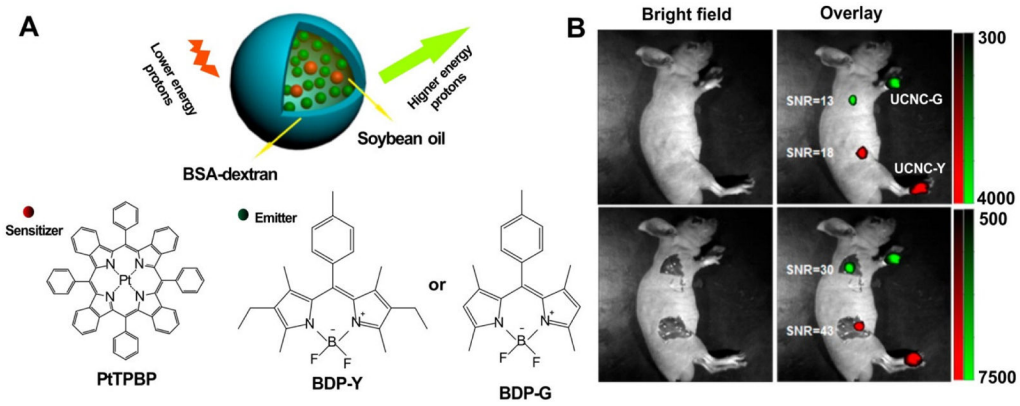

Figure 17.

TTA-UCNP composed of BSA–dextran stabilized oil droplets, co-loaded with PtTPBP and BDP dyes. A) The schematic illustration of TTA-UCNP composed of PtPBP (sensitizer) and BDP dyes (annihilator). The BSA–dextran stabilized oil droplets system enhanced the solubility of encapsulated agents. B) In vivo (top) and in situ (bottom) lymph node upconversion luminescence imaging of living mice at 30min after intradermal administration with the TTA-UCNP through paws (BDP-G for the forepaw and BDP-Y for the hindpaw). Permission obtained from Ref.[136]. Copyright (2013) by American Chemical Society.

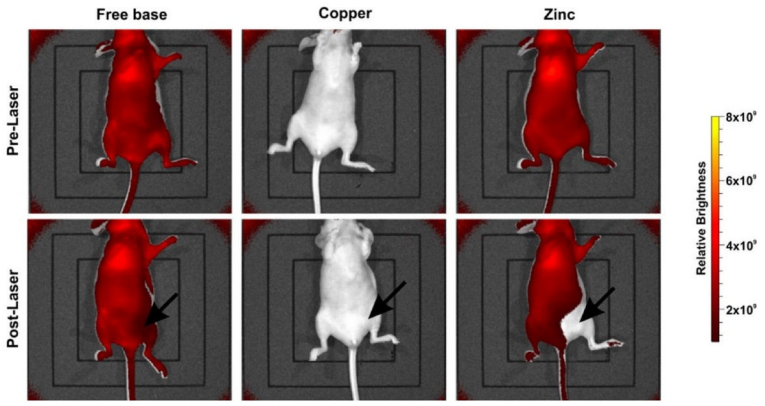

Figure 18.

In vivo imaging of HPPH-lipid fluorescence pre- and post-laser exposure. Mice were administrated intravenously equal doses (11 mg/kg) of three types HPPH-liposome and treated with a 665 nm laser at a fluence rate of 200 mW/cm^2 for 12.5 min (150 J/cm^2) 24 hours post-injection. The Cu-PoP did not show fluorescence and Zn-PoP showed a rapid self-bleaching. Permission obtained from Ref.[145]. Copyright (2016) by American Chemical Society.

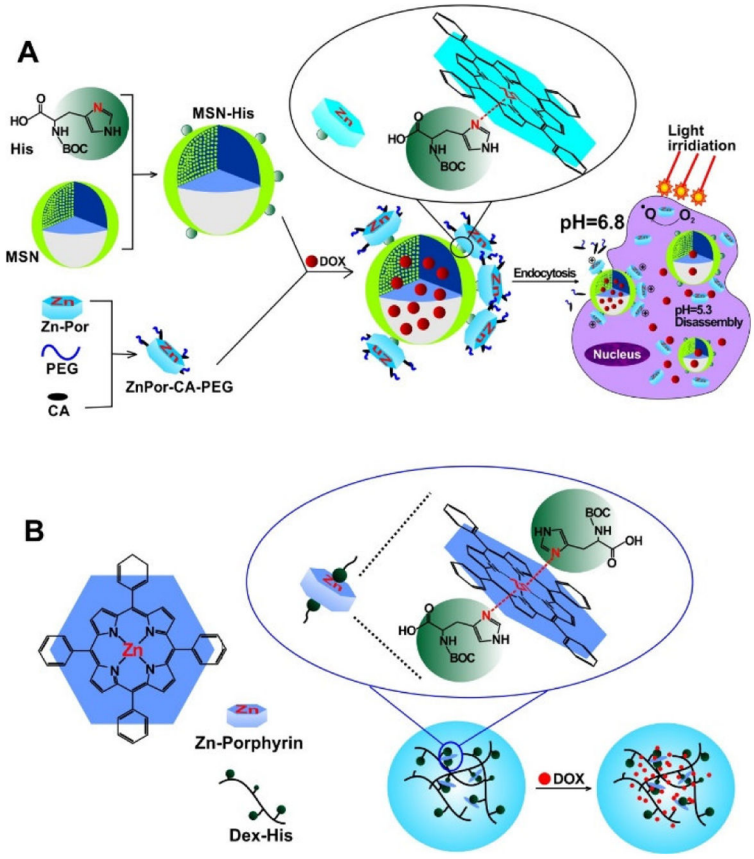

Figure 19.

pH sensitive metalloporphyrin NPs loaded with Dox. A) The schematic illustration of the dual pH sensitive mesoporous silica nanoparticle (MSN). ZnPor-CA-PEG formed the metallosupramolecular-coordination complex and attached on the MSN surface via the chelation between ZnPor and histidine. The bond between CA and ZnPor was cleaved in the extracellular environment where the pH ~6.8, resulting the positive charged nanoparticle and facile cellular internalization. In intracellular acidic microenvironments (pH~5.3), the chelation between histidine and ZnPor was broken and the encapsulated drug released. B) The structure of Dox loaded ZnPor supramolecular nanogel. Permission obtained from Ref. [51, 147]. Copyright by Elsevier and Royal Society of Chemistry.

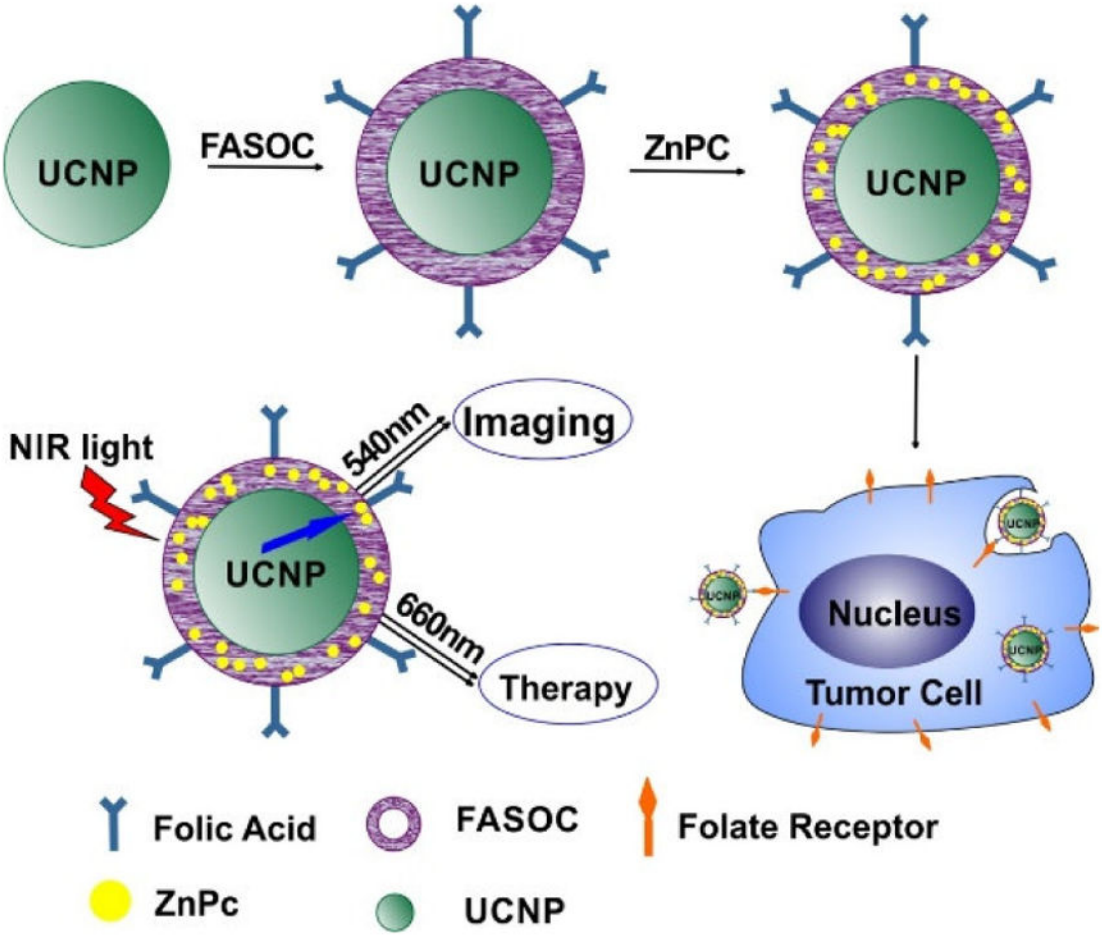

Figure 20.

Schematic illustration of preparation of FASOC-UCNP-ZnPC nanoparticles and folate-mediated binding to tumor cells. ZnPC was encapsulated into the FASCO-UNCP as the PDT agent. The UCNP absorbing 980nm light and activated the ZnPC which has a 660nm excitation wavelength. This nanoparticle could be uptaken specificly by the tumor cell overexpressing the folate receptor. Permission obtained from Ref.[154]. Copyright (2013) by American Chemical Society.

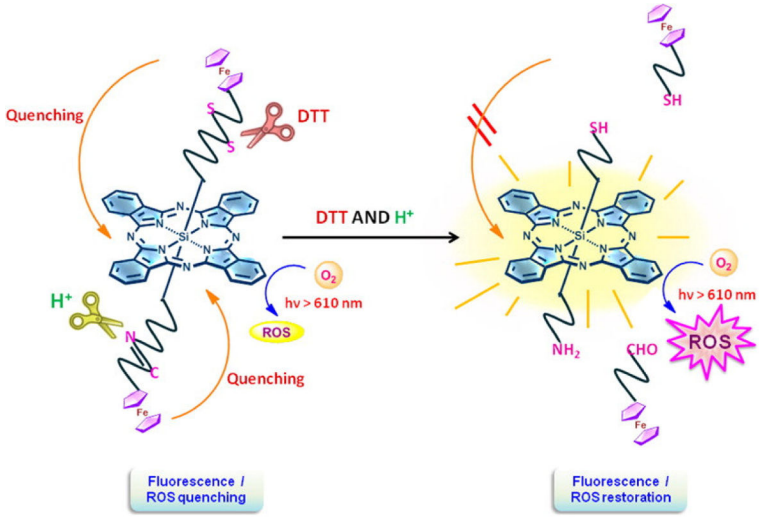

Figure 21.

A dual activatable photosensitizer. Si allows axial coordination of two different ligands for a dual activatable photosensitizer (DTT = dithiothreitol). Permission obtained from Ref.[155]. Copyright (2014) American Chemical Society.

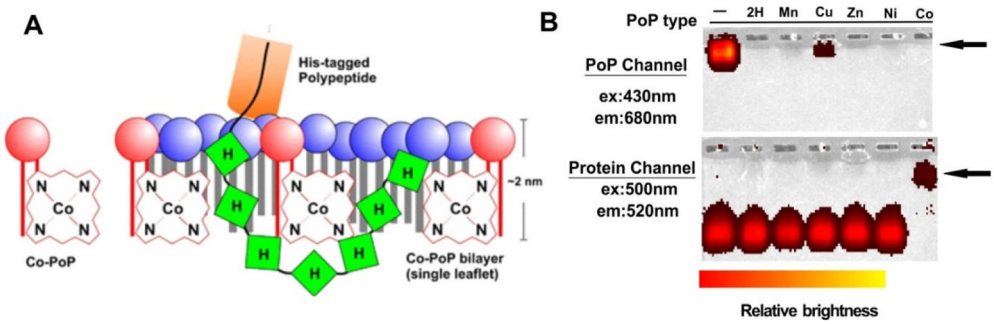

Figure 22.

Binding between CoPoP liposomes and his-tagged polypeptides. A) Schematic illustration of the his-tagged polypeptide binding with CoPoP. The his-tag is buried within the hydrophobic lipid bilayer. Only a single leaflet of the bilayer structure is shown. B) Stable binding between CoPoP liposomes and a his-tagged protein was demonstrated by the fluorescence imaging of a native electrophoresis gel. The arrows indicate the position of the liposomes. Only in the Co-PoP sample, the positions of CoPoP and protein coincided. Permission obtained from Ref.[156]. Copyright (2015) by Springer Nature.

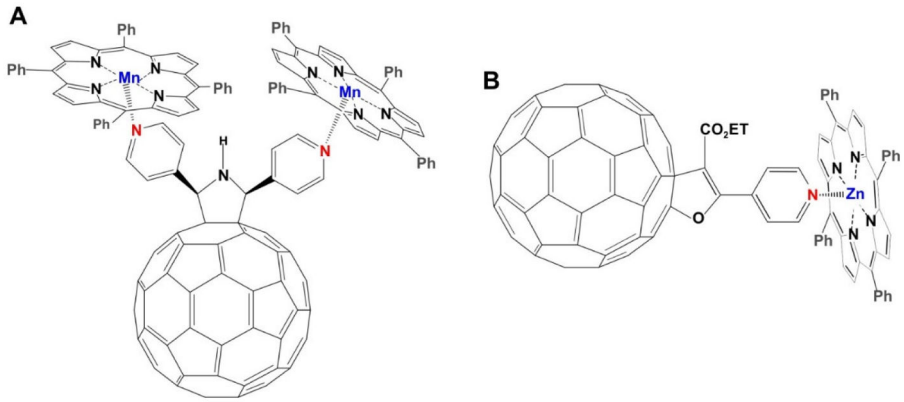

Figure 23.

The structure of a metalloporphyrin-fullerene compound. A) Structure of triad complex composed of DP3FP and two Mn^{II} TPP. Two pyridines were grafted on the surface of fullerene. The nitrogen atoms in pyridine further coordinated with Mn^{II} TPP and formed the triad complex. B) The structure of ZnTPPH-fullerene dyad used in the photoinduced H_2 evolution. Pyridine was conjugated on the surface of C_{60} and further occupied the axial coordination position of ZnTPPH as the ligand. This Zn-TPPH-fullerene dyad was applied for photoinduced H_2 evolution. Permission obtained from Ref.[169] and [170]. Copyright by Royal Society of Chemistry and American Chemical Society.

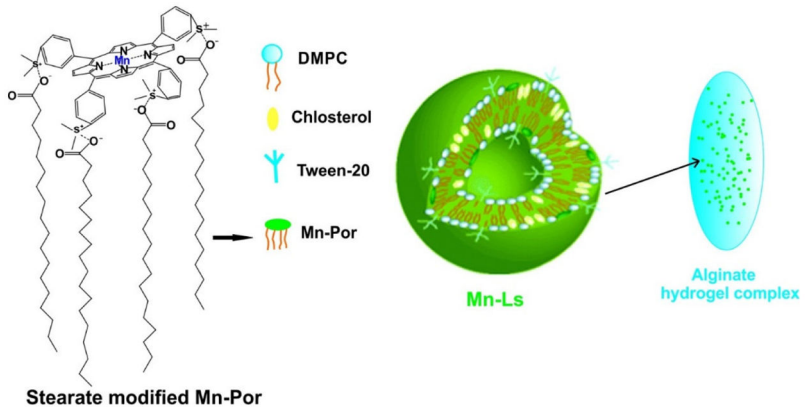

Figure 24.

Schematic illustration of a drug formulation for oral administration of a SOD mimic (Mn-Ls/Alg). The SOD agent, Mn-porphyrin (Mn-Ls), formed the liposome with DMPC and cholesterol. The liposome was encapsulated in alginate hydrogel matrix (Alg). Permission obtained from Ref.[178]. Copyright (2015) by Royal Society of Chemistry.

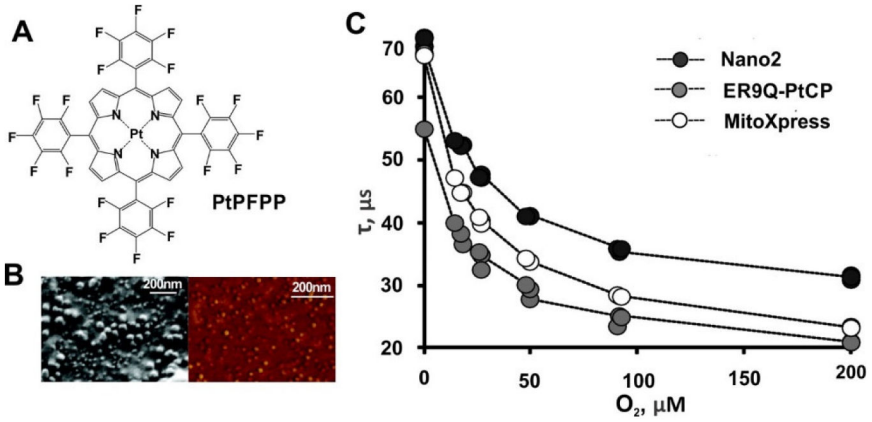

Figure 25.

Oxygen responsive Pt-porphyrin probes. A) The chemical structure of PtPFPP. B) The (Left) SEM and (Right) AFM images of the PtPFPP-RL100 NPs. C) Phosphorescence lifetime (τ) calibrations for three probes obtained with non-respiring MEF cells. ER9Q-PtCP, MitoXpress and Nano2 were design for monitoring the pericellular (PC), extracellular (EC), and intracellular (IC) O_2 concentrations, respectively. Permission obtained from Ref.[186]. Copyright (2012) by American Chemical Society.

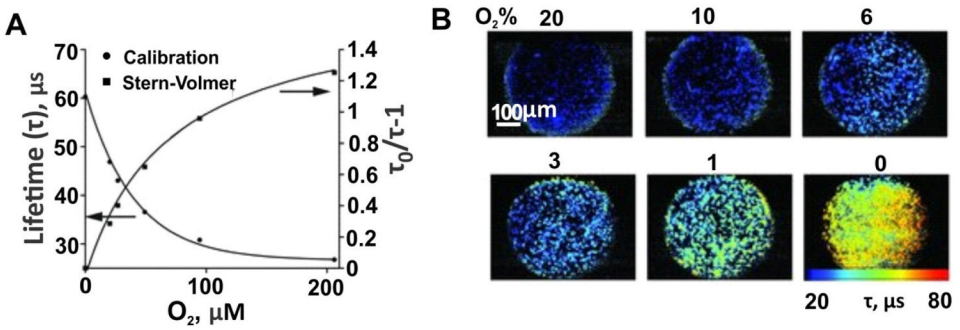

Figure 26.

Performance of a MM2 probe for sensing and imaging of icO_2. A) Phosphorescence lifetime calibration and Stern-Volmer plots of MM2 probe. B) Widefield fluorescence lifetime microscopy images of MEF cells stained with MM2 (10 μg mL^{-1}, 16 h). The images for different concentration of atmospheric O_2 were displayed. Permission obtained from Ref. [191] Copyright (2012) by Wiley.

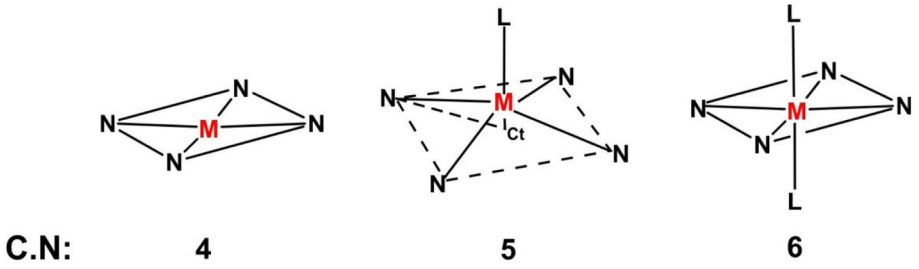

Scheme 1.

Different possible coordination geometries of metalloporpyrins. Ct = center of the ring, L=axial ligand, 4N = porphinato core, M = metal ion. Used with permission from Refs.[42, 43]. Copyright, American Chemical Society.